Geophysical Journal International

Geophys. J. Int. (2014) doi: 10.1093/gji/ggt517

Geophysical Journal International Advance Access published January 24, 2014

Accounting for prediction uncertainty when inferring subsurface fault slip

Zacharie Duputel,[1,*] Piyush S. Agram,[1,†] Mark Simons,[1] Sarah E. Minson[1] and James L. Beck[2]

[1]*Seismological Laboratory, California Institute of Technology,* 1200 *E California Blvd., Pasadena, CA* 91125-2100*, USA. E-mail: zacharie.duputel@unistra.fr*
[2]*Division of Engineering and Applied Science, California Institute of Technology,* 1200 *E California Blvd., Pasadena, CA 91125-2100, USA*

Accepted 2013 December 20. Received 2013 December 20; in original form 2013 August 1

SUMMARY

This study lays the groundwork for a new generation of earthquake source models based on a general formalism that rigorously quantifies and incorporates the impact of uncertainties in fault slip inverse problems. We distinguish two sources of uncertainty when considering the discrepancy between data and forward model predictions. The first class of error is induced by imperfect measurements and is often referred to as observational error. The second source of uncertainty is generally neglected and corresponds to the prediction error, that is the uncertainty due to imperfect forward modelling. Yet the prediction error can be shown to scale approximately with the size of earthquakes and thus can dwarf the observational error, particularly for large events. Both sources of uncertainty can be formulated using the misfit covariance matrix, $\mathbf{C}_\chi$, which combines a covariance matrix for observation errors, $\mathbf{C}_\mathrm{d}$ and a covariance matrix for prediction errors, $\mathbf{C}_\mathrm{p}$, associated with inaccurate model predictions. We develop a physically based stochastic forward model to treat the model prediction uncertainty and show how $\mathbf{C}_\mathrm{p}$ can be constructed to explicitly account for some of the inaccuracies in the earth model. Based on a first-order perturbation approach, our formalism relates $\mathbf{C}_\mathrm{p}$ to uncertainties on the elastic parameters of different regions (e.g. crust, mantle, etc.). We demonstrate the importance of including $\mathbf{C}_\mathrm{p}$ using a simple example of an infinite strike-slip fault in the quasi-static approximation. In this toy model, we treat only uncertainties in the 1-D depth distribution of the shear modulus. We discuss how this can be extended to general 3-D cases and applied to other parameters (e.g. fault geometry) using our formalism for $\mathbf{C}_\mathrm{p}$. The improved modelling of $\mathbf{C}_\mathrm{p}$ is expected to lead to more reliable images of the earthquake rupture, that are more resistant to overfitting of data and include more realistic estimates of uncertainty on inferred model parameters.

Key words: Inverse theory; Probability distributions; Earthquake source observations.

1 INTRODUCTION

Inferring earthquake source models is an essential ingredient in efforts to understand the physics of seismic rupture phenomena and the relationship of an earthquake with its tectonic and geodynamic environment. As such, the earthquake source model is not only an end into itself but serves as input into a variety of other related applications such as studies of fault zone rheology (e.g. Rice & Cocco 2007), earthquake energy budget analysis (e.g. Kanamori & Rivera 2006) and Coulomb stress transfer calculations (e.g. King 2007). Source estimates are also useful for rapid assessment and response to seismic disasters when they occur (e.g. Duputel *et al.* 2012b). However, source inversion algorithms usually do not include realistic error analyses and their results are generally not accompanied by reliable estimates of uncertainty. These limitations reduce the utility of inferred rupture models and associated by-products. Furthermore, uncertainty in both data and model predictions can cause current source models to be significantly biased due to overfitting of seismic and geodetic observations.

Descriptions of earthquake sources come in various flavours depending on the nature of the data (e.g. seismological, geodetic, geological), the observation scale (i.e. regional or global), the

*Now at: Institut de Physique du Globe de Strasbourg, UdS and EOST/CNRS UMR 7516, France.
†Now at: Jet Propulsion Laboratory, California Institute of Technology, Pasadena, California 91109, USA.

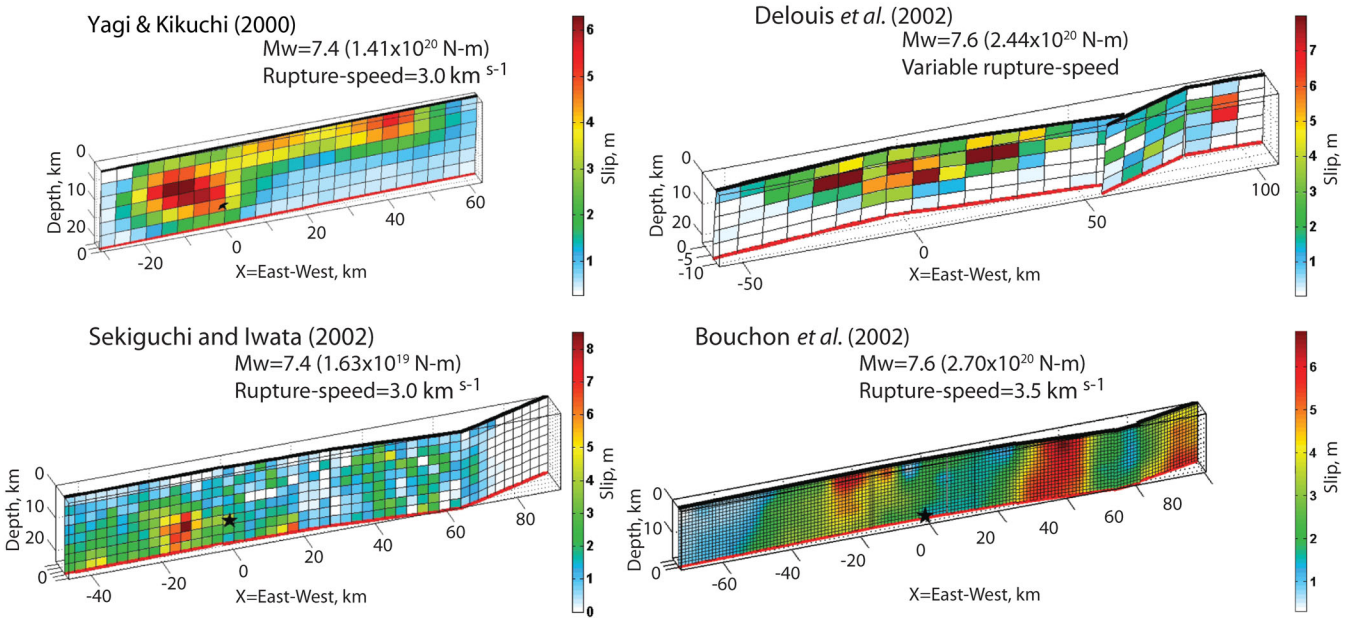

Figure 1. An illustration of variability of kinematic earthquake source models. Results of finite-source rupture modelling obtained by different research groups are presented for the 1999 Izmit earthquake (Yagi & Kikuchi 2000; Bouchon *et al.* 2002; Delouis *et al.* 2002; Sekiguchi & Iwata 2002). The origin of *XY*-coordinates is set at the epicentre location. These source models are available through the SRCMOD source inversion database (Mai 2012).

parametrization of the source (e.g. linear versus non-linear) and the approach used to infer relevant parameters (e.g. Yabuki & Matsu'ura 1992; Wald & Heaton 1994; Ji *et al.* 2002; Minson *et al.* 2013). The reliability of any source inversion depends on many factors including the size and complexity of the event, the amount and quality of data, the way in which data sample the source region and, while usually disregarded, uncertainties in our forward models (i.e. our model predictions).

The last decade has seen considerable improvements in the fidelity of forward modelling capability (e.g. Komatitsch & Vilotte 1998; Williams *et al.* 2005) and a substantial expansion of geophysical observations including broad-band data from dense seismic networks (e.g. USArray, http://www.usarray.org; Geonet, http://geonet.org.nz; CENC, http://www.csndmc.ac.cn; F-net, Okada *et al.* 2004), continuously recording geodetic positioning data from permanent GPS installations (e.g. the Plate Boundary Observatory, http://pbo.unavco.org; Geonet, http://geonet.org.nz, Taiwan GPS Network, Yu *et al.* 1997) and spatially synoptic geodetic imaging data from orbiting radar and optical satellites (e.g. Simons & Rosen 2007). Despite this progress in forward modelling and data acquisition, one of the biggest obstacles to significant progress in earthquake source modelling arises from imperfect predictions of geodetic and seismic data due to uncertainties in (or imperfect knowledge of) the Earth structure—whose impact is generally ignored. Indeed, for large earthquakes and even aseismic processes, our ability to measure ground motions frequently far exceeds our ability to model them. As discussed latter in Section 2 for linear elastic deformation, the prediction errors due to earth model inaccuracies scale with the fault slip. This aspect is particularly important since large events with large amounts of slip will magnify earth model errors in contrast to small earthquakes for which measurement errors are dominant. Besides the necessity to continue improving the accuracy and efficiency of forward calculations, one of the main challenges today is thus to develop an accurate stochastic model that better describes modelling uncertainty in predicting geodetic and seismic data.

One approach to estimate the uncertainty in source parameters for a given earthquake is to compare fault slip models obtained by various research groups using different inversion approaches (Mai 2012). Fig. 1 shows selected kinematic rupture models for the 1999 Izmit earthquake. Although these models are generally derived from similar data sets, there is a large variability in inversion results. The 1999 Izmit earthquake is not an isolated case. For many events, such as the 1992 Landers or 2001 Arequipa earthquakes, small differences in modelling techniques and data lead to striking differences in inferred slip models (Wald & Heaton 1994; Hernandez *et al.* 1999; Pritchard *et al.* 2007). When different methodologies yield different results for the same event, it is not obvious how any conclusion about the rupture process can be drawn.

This study focus on theoretical and algorithmic developments needed for the next generation of finite-fault earthquake source models by providing a general formalism to explicitly quantify the impact of uncertainties in our forward models and to rigorously incorporate such uncertainties in large ill-posed source inversion problems. We stress the importance of using a stochastic forward modelling approach in this process. It allows us to describe a probability distribution of predictions for a given source model, contrary to a deterministic approach that provides a single set of (potentially inaccurate) predictions. This idea of incorporating stochastic (probabilistic) models in the inverse problem is not new and was introduced in geophysics around 1980, notably by Tarantola & Valette (1982). More recently, Yagi & Fukahata (2011) used such a formalism and proposed a stochastic forward model based on adding Gaussian noise to the unattenuated 1-D teleseismic Green's functions. This Gaussian noise is characterized by a covariance matrix that is partially specified *a priori*. Minson *et al.* (2013) also presented a Gaussian model for the uncertain prediction error in the forward modelling, taking a diagonal covariance matrix with variances that scale with the square of observed amplitudes. In the two approaches, the scale factor that controls the prediction-error variances is incorporated in the model parameters to be inverted. Based on these early studies, we develop here a new formulation exploiting more of the

physics of the forward problem to improve the modelling of the prediction covariance matrix. This general formalism can be used for various problems (e.g. earthquake or volcanic source inversions based on seismic or geodetic data) and relates input uncertainties in the earth model or source geometry to the corresponding distribution of predictions. As recognized by Yagi & Fukahata (2011) and Minson *et al.* (2013), a physically based stochastic model must also account for the dependence of the prediction uncertainty upon the slip model.

We begin by developing the concept of the misfit covariance matrix as used in inversions of slip on subsurface faults. This matrix is the sum of a covariance matrix for observations (often assumed independent) and a covariance matrix for prediction errors associated with inaccurate model predictions (often entirely ignored). We then describe how a physically informed prediction covariance matrix can be obtained. In particular, we consider the effect of uncertainties in the earth model. Our description is based on a Bayesian formulation of the inverse problem but our formalism can also be used in optimization methods. Although our approach is general and can be used for various seismic and geodetic data sets, we explore here the advantage of including more structured reasonable prediction covariance matrices by using simple quasi-static models. We also discuss how to account for other sources of prediction uncertainty such inaccurate as fault geometries. Given the increased computational complexity, we leave a similar development of the prediction covariance for kinematic modelling to a future study.

2 ON THE IMPORTANCE OF PREDICTION UNCERTAINTY IN SOURCE INVERSION PROBLEMS

Let $\mathbf{d}_{\rm obs} = [d_1^{\rm obs}, d_2^{\rm obs}, \ldots, d_N^{\rm obs}]^T$ be the set of N field observations used in the source inversion process. Let also define $\mathbf{m}$ as the set of source model parameters in the M-dimensional model space $\mathfrak{M}$. In the source inversion process, we want to use $\mathbf{d}_{\rm obs}$ to learn about $\mathbf{m}$. As in many inverse problems, error models play a central role in the formulation of uncertainties and our knowledge of $\mathbf{m}$ will strongly depend on the information they provide. In our problem, we can separate two sources of error that we can account for using appropriate stochastic models. These two fundamental probability models are discussed in the following.

The first source of uncertainty comes from the observational error that is induced by the measurement process. When measuring an N-dimensional quantity $\mathbf{d}$, measurements are associated with an uncertain error $\mathbf{e}$ given by

$$\mathbf{e} = \mathbf{d}^* - \mathbf{d}. \tag{1}$$

In this equation, $\mathbf{d}^*$ is a stochastic variable representing uncertain measurement and $\mathbf{d}$ is the actual displacement value. The set of field observations $\mathbf{d}_{\rm obs} = [d_1^{\rm obs}, d_2^{\rm obs}, \ldots, d_N^{\rm obs}]^T$ can be seen as a single realization of $\mathbf{d}^*$. In other words, $\mathbf{d}_{\rm obs}$ is a fixed vector corresponding to actual measured values and $\mathbf{d}^*$ is a stochastic vector representing uncertainty on those field observations. We will assume that positive and negative errors of equal magnitude are equally plausible and so take $\mathbf{e}$ to have zero mean. We also choose a covariance matrix $\mathbf{C}_{\rm d}$ for $\mathbf{e}$. Following the Principle of Maximum Entropy (Jaynes 1983, 2003), the probability density function (PDF) that assumes the least additional information about $\mathbf{e}$ under these conditions is a Gaussian probability density $p(\mathbf{e}|\mathbf{d}) = \mathcal{N}(\mathbf{e}|\mathbf{0}, \mathbf{C}_{\rm d})$ with covariance matrix $\mathbf{C}_{\rm d}$ and zero mean (*cf.* Bishop 2006). Our stochastic model for the measurement process is thus given by

$$p(\mathbf{d}^*|\mathbf{d}) = \mathcal{N}(\mathbf{d}^*|\mathbf{d}, \mathbf{C}_{\rm d}) = \frac{1}{\sqrt{(2\pi)^N |\mathbf{C}_{\rm d}|}} \exp\left(-\frac{1}{2}(\mathbf{d}^* - \mathbf{d})^T \mathbf{C}_{\rm d}^{-1} (\mathbf{d}^* - \mathbf{d})\right), \tag{2}$$

where $p(\mathbf{d}^*|\mathbf{d})$ is the probability (density) for getting the measured value $\mathbf{d}^*$ when the uncertain physical quantity being measured has the value $\mathbf{d}$. The PDF $p(\mathbf{d}^*|\mathbf{d})$ and the associated measurement covariance matrix $\mathbf{C}_{\rm d}$ depend of course on the nature of measurement and on the type of instrument used. A common model is to take independent observational errors (i.e. diagonal $\mathbf{C}_{\rm d}$). However, for observations like InSAR or seismic data, off-diagonal components should be included in $\mathbf{C}_{\rm d}$ to allow correlation of measurement errors between neighbouring data samples (e.g. Lohman & Simons 2005; Fukahata & Wright 2008; Duputel *et al.* 2012a).

The second source of uncertainty corresponds to our imperfect knowledge of $\mathbf{d}$ for a given source model $\mathbf{m}$, which comes from the prediction error due to imperfect forward modelling, also referred to as epistemic error. For earthquake source modelling problems, this component includes but is not limited to, lack of fidelity in the fault geometry, oversimplifications of the mechanical earth model and approximations made when calculating the Earth's response to an applied force.

Let $\mathbf{g}(\boldsymbol{\Psi}, \mathbf{m})$ be a deterministic model for the forward predictions for a source model $\mathbf{m}$. In addition to the source model, the forward model depends on a set of uncertain properties parametrized by a vector $\boldsymbol{\Psi}$ that is not solved for (e.g. earth model elastic properties, fault geometry). We are uncertain about what value to take for the parameters $\boldsymbol{\Psi}$. Suppose $\widetilde{\boldsymbol{\Psi}}$ denotes the most plausible value *a priori*. Then, for a given source model $\mathbf{m}$, we obtain the corresponding prediction $\mathbf{d}_{\rm pred} = \mathbf{g}(\widetilde{\boldsymbol{\Psi}}, \mathbf{m})$. We define the uncertain prediction error by

$$\boldsymbol{\epsilon} = \mathbf{d} - \mathbf{d}_{\rm pred} = \mathbf{d} - \mathbf{g}(\widetilde{\boldsymbol{\Psi}}, \mathbf{m}), \tag{3}$$

which is taken as a stochastic variable associated with a probability density $p(\boldsymbol{\epsilon}|\mathbf{m})$, that describes the uncertainty in the actual physical quantity $\mathbf{d}$ (i.e. displacement), given $\mathbf{d}_{\rm pred}$. Using a similar argument for $\boldsymbol{\epsilon}$ as for $\boldsymbol{e}$ above, we choose a maximum entropy distribution subject to a zero mean and a covariance matrix $\mathbf{C}_{\rm p}(\mathbf{m})$ to get the Gaussian distribution $p(\boldsymbol{\epsilon}|\mathbf{m}) = \mathcal{N}[\boldsymbol{\epsilon}|\mathbf{0}, \mathbf{C}_{\rm p}(\mathbf{m})]$. The corresponding stochastic forward model for the predictions is then given by the conditional Gaussian PDF

$$p(\mathbf{d}|\mathbf{m}) = \mathcal{N}\left[\mathbf{d}|\mathbf{g}(\widetilde{\boldsymbol{\Psi}}, \mathbf{m}), \mathbf{C}_{\rm p}(\mathbf{m})\right] = \frac{1}{\sqrt{(2\pi)^N \left|\mathbf{C}_{\rm p}(\mathbf{m})\right|}} \times \exp\left(-\frac{1}{2}\left[\mathbf{d} - \mathbf{g}(\widetilde{\boldsymbol{\Psi}}, \mathbf{m})\right]^T \mathbf{C}_{\rm p}(\mathbf{m})^{-1} \left[\mathbf{d} - \mathbf{g}(\widetilde{\boldsymbol{\Psi}}, \mathbf{m})\right]\right). \tag{4}$$

Even though the prediction error is generally neglected (i.e. $\mathbf{C}_{\rm p} = \mathbf{0}$), we know that its contribution can be comparable or even larger than measurement errors, in particular for large earthquakes. This can be easily understood if we consider, for example, a linear formulation of the forward problem $\mathbf{g}(\boldsymbol{\Psi}, \mathbf{m}) = \mathbf{G}(\boldsymbol{\Psi}) \cdot \mathbf{m}$. In this case, we can write

$$\boldsymbol{\epsilon} = \left[\mathbf{G}(\boldsymbol{\Psi}) - \mathbf{G}(\widetilde{\boldsymbol{\Psi}})\right] \cdot \mathbf{m} = \boldsymbol{\Gamma}(\widetilde{\boldsymbol{\Psi}}, \boldsymbol{\Psi}) \cdot \mathbf{m}, \tag{5}$$

where the matrix $\boldsymbol{\Gamma}$ describes the uncertainty in $\mathbf{G}$ due to the uncertainty in $\boldsymbol{\Psi}$. In this equation, the level of the prediction error $\boldsymbol{\epsilon}$ modelled by $\mathbf{C}_{\rm p}$ scales with the magnitude of the source model

$\mathbf{m}$ (this dependence is also discussed in Yagi & Fukahata 2011). The observational uncertainties, on the other hand, are independent of the model parameters and are essentially controlled by the nature and quality of the measurements. For large earthquakes, the contribution of $\mathbf{C}_d$ is thus frequently negligible compared to $\mathbf{C}_p$.

At this point, we therefore have (1) a stochastic model $p(\mathbf{d}^*|\mathbf{d})$ associated with $\mathbf{C}_d$ in eq. (2) describing the measurement uncertainty and (2) a stochastic forward model $p(\mathbf{d}|\mathbf{m})$ associated with $\mathbf{C}_p$ in eq. (4) describing the prediction uncertainty. Using Bayesian source inversion, our goal here is to combine the available information from observations and prior information about the model parameters and forward modelling to construct a posterior distribution for the source model parameters. To do so, we use Bayes' theorem to get the posterior PDF $p(\mathbf{m}|\mathbf{d}_{obs})$ over the model space (Bayes 1763):

$$p(\mathbf{m}|\mathbf{d}_{obs}) = \kappa\ p(\mathbf{d}_{obs}|\mathbf{m})\ p(\mathbf{m}), \tag{6}$$

where κ is a normalization constant and $p(\mathbf{d}_{obs}|\mathbf{m})$ is a likelihood function:

$$p(\mathbf{d}_{obs}|\mathbf{m}) = \int_{\mathfrak{D}_{pred}} p(\mathbf{d}_{obs}|\mathbf{d})\ p(\mathbf{d}|\mathbf{m})\,\mathrm{d}\mathbf{d}. \tag{7}$$

Strictly speaking, $p(\mathbf{d}_{obs}|\mathbf{m})$ is a marginal or integrated likelihood in which $\mathbf{d}$ has been marginalized out over the prediction space $\mathfrak{D}_{pred}$, which is the space of all conceivable forward model predictions. Eq. (6) states that the posterior probability density of $\mathbf{m}$ given the measurements $\mathbf{d}_{obs}$ is proportional to the product of a PDF $p(\mathbf{m})$ describing the prior information on $\mathbf{m}$ and the likelihood function $p(\mathbf{d}_{obs}|\mathbf{m})$, which gives a measure of how well the model $\mathbf{m}$ explains the data $\mathbf{d}_{obs}$. A similar result can be obtained using the concept of conjunction of states of information as introduced by Tarantola & Valette (1982). In eq. (7), $p(\mathbf{d}_{obs}|\mathbf{d})$ comes from substituting $\mathbf{d}^* = \mathbf{d}_{obs}$ in the probability model $p(\mathbf{d}^*|\mathbf{d})$. It describes the likelihood of having observed $\mathbf{d}_{obs}$ if the actual displacement was $\mathbf{d}$. Using the stochastic models developed in eqs (2) and (4) in eqs (6) and (7), we can then show (*cf.* Appendix A)

$$p(\mathbf{m}|\mathbf{d}_{obs}) = \eta(\mathbf{m})\ p(\mathbf{m})\ \exp\left(-\frac{1}{2}\left[\mathbf{d}_{obs} - \mathbf{g}(\widetilde{\boldsymbol{\Psi}}, \mathbf{m})\right]^T \times\ \mathbf{C}_\chi(\mathbf{m})^{-1}\left[\mathbf{d}_{obs} - \mathbf{g}(\widetilde{\boldsymbol{\Psi}}, \mathbf{m})\right]\right), \tag{8}$$

where $\mathbf{C}_\chi(\mathbf{m})$ is the misfit covariance matrix defined as

$$\mathbf{C}_\chi(\mathbf{m}) = \mathbf{C}_d + \mathbf{C}_p(\mathbf{m}) \tag{9}$$

and $\eta(\mathbf{m})$ is a normalization factor:

$$\eta(\mathbf{m}) = \kappa\ (2\pi)^{-N/2}\ |\mathbf{C}_d|^{-1/2}\ \left|\mathbf{C}_p(\mathbf{m})\right|^{-1/2}\ \left|\mathbf{C}_d^{-1} + \mathbf{C}_p(\mathbf{m})^{-1}\right|^{-1/2}. \tag{10}$$

It is important to note that the covariance $\mathbf{C}_\chi$ plays a central role in the inversion process. First of all, $\mathbf{C}_\chi$ controls the shape of the posterior probability density $p(\mathbf{m}|\mathbf{d}_{obs})$ and therefore affects the solution of the inverse problem. Secondly, $\mathbf{C}_\chi$ is the only term in eq. (8) that describes the statistics of measurement ($\mathbf{C}_d$) and model prediction errors ($\mathbf{C}_p$). Among these two contributors, $\mathbf{C}_d$ can easily be more readily taken into account because the statistics of observational uncertainties are generally well characterized. $\mathbf{C}_p$, on the other hand, is usually neglected even if its contribution can be larger than $\mathbf{C}_d$ as discussed above. In this paper, we advocate improved modelling of the prediction-error uncertainty in any source inversion problem by developing a stochastic forward model using a covariance matrix structure based on an explicit treatment of uncertainties in the predictions.

3 A STOCHASTIC MODEL FOR THE PREDICTION UNCERTAINTY

The development of a covariance matrix for the predictions ($\mathbf{C}_p$) is important regardless of the particular approach one uses to invert for source model parameters. Indeed, in most source inversion problems (e.g. Hartzell & Heaton 1983; Delouis *et al.* 2000; Ji *et al.* 2002; Simons *et al.* 2011; Minson *et al.* 2013, 2014), the discrepancies between data $\mathbf{d}_{obs}$ and forward predictions $\mathbf{g}(\widetilde{\boldsymbol{\Psi}}, \mathbf{m})$ for a source model $\mathbf{m}$ are quantified by defining a least-squares misfit function of the form

$$\chi(\mathbf{m}) = \frac{1}{2}\left[\mathbf{d}_{obs} - \mathbf{g}(\widetilde{\boldsymbol{\Psi}}, \mathbf{m})\right]^T \cdot \mathbf{C}_\chi^{-1} \cdot \left[\mathbf{d}_{obs} - \mathbf{g}(\widetilde{\boldsymbol{\Psi}}, \mathbf{m})\right]. \tag{11}$$

In a parameter optimization process, $\chi(\mathbf{m})$ is minimized while in a Bayesian formulation the likelihood function is given by $p(\mathbf{d}_{obs}|\mathbf{m}) = \eta(\mathbf{m})\exp(-\chi(\mathbf{m}))$. Therefore, whatever the source estimation method, a central role is played by the misfit covariance matrix, $\mathbf{C}_\chi = \mathbf{C}_d + \mathbf{C}_p$. As we discussed previously, $\mathbf{C}_p$ is the dominant term for large earthquakes and the construction of an improved prediction covariance matrix can lead to improved source imaging techniques. If one adopts a regularized least-squares approach for finite-fault models using a Tikhonov regularization (e.g. minimum moment, minimum roughness), then the particular choice of the penalty parameter depends on the effective information content of the data. This dependence on $\mathbf{C}_\chi$ is true regardless of whether one chooses the amount of damping by some L-curve approach, cross-validation or Bayesian model class selection. Similarly, if one chooses to adopt a fully Bayesian approach, then having the appropriate covariance matrix can control the extent to which one does or does not overfit the observations.

3.1 Prediction uncertainty due to inaccuracies in the forward model

The derivation proposed here is developing ideas proposed by Duputel *et al.* (2012a), who demonstrated that centroid location uncertainty in point-source moment tensor inversions can be accounted for by designing a prediction covariance matrix $\mathbf{C}_p$ based on the relevant physics of the forward problem. In this study, we consider the effects of properties of the forward model which are not solved for but can significantly affect the predictions (e.g. Earth elastic properties, fault geometry).

Hereafter, we derive the statistics of the prediction uncertainty by assuming that $\mathbf{g}(\boldsymbol{\Psi}, \mathbf{m})$ for given generic properties $\boldsymbol{\Psi}$ of the forward model is well approximated by linearized perturbations of our predictions $\mathbf{g}(\widetilde{\boldsymbol{\Psi}}, \mathbf{m})$ for the *a priori* set of parameters $\widetilde{\boldsymbol{\Psi}}$:

$$\mathbf{g}(\boldsymbol{\Psi}, \mathbf{m}) \approx \mathbf{g}(\widetilde{\boldsymbol{\Psi}}, \mathbf{m}) + \mathbf{K}_\Psi(\widetilde{\boldsymbol{\Psi}}, \mathbf{m}) \cdot (\boldsymbol{\Psi} - \widetilde{\boldsymbol{\Psi}}), \tag{12}$$

where the matrix $\mathbf{K}_\Psi(\widetilde{\boldsymbol{\Psi}}, \mathbf{m})$ is the so-called sensitivity kernel of the predictions with respect to $\boldsymbol{\Psi}$:

$$(\mathbf{K}_\Psi)_{ij}(\widetilde{\boldsymbol{\Psi}}, \mathbf{m}) = \frac{\partial g_i}{\partial \Psi_j}(\widetilde{\boldsymbol{\Psi}}, \mathbf{m}). \tag{13}$$

Under the first-order approximation of eq. (12), we can write the prediction error $\boldsymbol{\epsilon}$ as

$$\boldsymbol{\epsilon} = \mathbf{g}(\boldsymbol{\Psi}, \mathbf{m}) - \mathbf{g}(\widetilde{\boldsymbol{\Psi}}, \mathbf{m}) \approx \mathbf{K}_\Psi(\widetilde{\boldsymbol{\Psi}}, \mathbf{m}) \cdot \delta\boldsymbol{\Psi}. \tag{14}$$

Using eq. (12) we can write Jacobian rule $p(\mathbf{\Psi}) = p(\mathbf{d}|\mathbf{m})|\frac{\partial \mathbf{d}}{\partial \mathbf{\Psi}}|$, where $|\frac{\partial \mathbf{d}}{\partial \mathbf{\Psi}}|$ is the Jacobian determinant of the transformation $\mathbf{d} = \mathbf{g}(\mathbf{\Psi})$ and we write the prediction covariance as

$$\mathbf{C}_\mathrm{p}(\mathbf{m}) = \int \left[\mathbf{g}(\mathbf{\Psi}, \mathbf{m}) - \mathbf{g}(\widetilde{\mathbf{\Psi}}, \mathbf{m})\right] \times \left[\mathbf{g}(\mathbf{\Psi}, \mathbf{m}) - \mathbf{g}(\widetilde{\mathbf{\Psi}}, \mathbf{m})\right]^T \; p(\mathbf{\Psi})\, \mathrm{d}\mathbf{\Psi}, \tag{15}$$

where $p(\mathbf{\Psi})$ is the prior probability density describing the uncertainty in the generic properties $\mathbf{\Psi}$. We assume here that $p(\mathbf{\Psi})$ is a Gaussian distribution:

$$p(\mathbf{\Psi}) = \mathcal{N}(\mathbf{\Psi}|\widetilde{\mathbf{\Psi}}, \mathbf{C}_\Psi), \tag{16}$$

which corresponds to the least informative PDF that is adequate for given *a priori* parameters $\widetilde{\mathbf{\Psi}}$ and a covariance matrix $\mathbf{C}_\Psi$ defined as

$$\mathbf{C}_\Psi = \int (\mathbf{\Psi} - \widetilde{\mathbf{\Psi}})(\mathbf{\Psi} - \widetilde{\mathbf{\Psi}})^T \; p(\mathbf{\Psi})\, \mathrm{d}\mathbf{\Psi}. \tag{17}$$

If more information is available about $\mathbf{\Psi}$, one can of course choose another more informative form of $p(\mathbf{\Phi})$. By plugging eqs (14) and (17) into eq. (15), it follows that

$$\mathbf{C}_\mathrm{p} = \mathbf{K}_\Psi \cdot \mathbf{C}_\Psi \cdot \mathbf{K}_\Psi^T, \tag{18}$$

where we drop the variables $\widetilde{\mathbf{\Psi}}$ and $\mathbf{m}$ for clarity. Using the formulation developed above, we can do much better than predicting a set of observations for a given source model. We can now construct a probability distribution for the predictions $p(\mathbf{d}|\mathbf{m}) = \mathcal{N}[\mathbf{d}|\mathbf{g}(\widetilde{\mathbf{\Psi}}, \mathbf{m}), \mathbf{C}_\mathrm{p}]$, that is, a stochastic forward model based on more of the physics of the problem and reflecting uncertainties in properties $\mathbf{\Psi}$ which are not inverted but can affect the predictions.

3.2 Accounting for inaccuracies in the earth model

Among the different sources of uncertainty, the approximate nature of the chosen earth model is of great interest as it is one of the largest contributors to forward modelling errors (Savage 1987; Hjörleifsdóttir & Ekström 2010; Yagi & Fukahata 2011). We explicitly treat this aspect in constructing a stochastic forward model for $\mathbf{d}$. In some extreme cases, an earth model $\widetilde{\mathbf{\Omega}}$ can be very different from the actual elastic structure and there will be no simple relationship between the corresponding predictions and the actual displacement values. In such situations, results of our inversion would be unreliable and we should focus our efforts on obtaining a more accurate earth model. However, in most applications, elastic models are reasonable approximations of the true underlying elastic structure of the Earth and we may still be able to solve the source inversion problem by designing an appropriate misfit covariance model, $\mathbf{C}_\chi$.

As in previous section, we can derive the statistics of the prediction uncertainty by assuming that $\mathbf{g}(\mathbf{\Omega}, \mathbf{m})$ for given elastic parameters $\mathbf{\Omega}$ is well approximated by linearized perturbations of our predictions $\mathbf{g}(\widetilde{\mathbf{\Omega}}, \mathbf{m})$ for the *a priori* earth model $\widetilde{\mathbf{\Omega}}$. The elastic parameters in $\mathbf{\Omega}$ being strictly positive, we use the formulation described in Section 3.1 with $\mathbf{\Psi} = \ln \mathbf{\Omega}$. We therefore assume here that $p(\mathbf{\Omega})$ is a log-normal distribution which corresponds to the least-informative PDF (i.e. the maximum entropy PDF) that is adequate for a Jeffrey's parameter (Tarantola 2005):

$$p(\ln \mathbf{\Omega}) = \mathcal{N}(\ln \mathbf{\Omega}|\ln \widetilde{\mathbf{\Omega}}, \mathbf{C}_\Omega), \tag{19}$$

with $\ln \widetilde{\mathbf{\Omega}}$ and $\mathbf{C}_\Omega$, respectively, the mean and covariance of $\ln \mathbf{\Omega}$. This choice of a log-normal distribution is also justified by the fact that modern tomography techniques are often based on relative model perturbations (e.g. $\delta \ln \Omega = \delta\Omega/\Omega$, Tromp *et al.* 2005). The prediction covariance matrix associated with such uncertainty in the earth model is then given by

$$\mathbf{C}_\mathrm{p} = \mathbf{K}_\Omega \cdot \mathbf{C}_\Omega \cdot \mathbf{K}_\Omega^T, \tag{20}$$

where the matrix $\mathbf{K}_\Omega$ is the sensitivity kernel of the predictions with respect to the earth model parameters:

$$(\mathbf{K}_\Omega)_{ij}(\widetilde{\mathbf{\Omega}}, \mathbf{m}) = \frac{\partial g_i}{\partial \ln \Omega_j}(\widetilde{\mathbf{\Omega}}, \mathbf{m}). \tag{21}$$

In Section 4, we consider a simple 1-D case for which Ω_j represents the shear modulus μ_j in the jth layer of the tabular elastic model $\widetilde{\mathbf{\Omega}} = \widetilde{\boldsymbol{\mu}}$ used to compute the predictions $g_i(\widetilde{\boldsymbol{\mu}}, \mathbf{m})$. In the 3-D case, $\Omega_j = \mu_j$ can represent the shear modulus in the jth region of the earth model (*cf.* Appendix B).

3.3 Practical implementation in a Bayesian framework

In this study, we use a Bayesian sampling algorithm called Cascading Adaptive Transitional Metropolis In Parallel (CATMIP), which allows sampling in very high dimensional problems in a parallel computing framework (Minson *et al.* 2013). CATMIP combines the Metropolis algorithm with elements of simulated annealing and genetic algorithms to dynamically optimize the algorithms efficiency as it runs. As proposed initially by Beck & Au (2002) and Ching & Chen (2007), the CATMIP algorithm samples from a series of intermediate PDFs:

$$f(\mathbf{m}, \beta_i) \propto p(\mathbf{m})\; p(\mathbf{d}_\mathrm{obs}|\mathbf{m})^\beta, \quad i = 1, \ldots, B \quad 0 = \beta_0 < \beta_1 < \beta_2 < \ldots < \beta_B = 1. \tag{22}$$

In this procedure, we start at $\beta_0 = 0$ to sample the prior and slowly increase β_i through several transitional steps. When $\beta_i = \beta_B = 1$, we obtain an accurate sampling of the posterior probability density $p(\mathbf{m}|\mathbf{d}_\mathrm{obs})$. As proposed in Ching & Chen (2007) and Beck & Zuev (2013), we optimize the transitional process by choosing each $\delta\beta_i = \beta_{i+1} - \beta_i$ adaptively rather than using a pre-set schedule for the sequence of β_i. More specifically, each $\delta\beta_i$ is chosen such that the effective sample size between $f(\mathbf{m}, \beta_i)$ and $f(\mathbf{m}, \beta_{i+1})$ is about 50 per cent (Beck & Zuev 2013). Between each transitional step, a large number of Markov chains run in parallel. Each chain is governed by the Metropolis algorithm in which the probability of acceptance of one candidate sample is determined by comparing the value of the intermediate PDF with that of the current sample (Minson *et al.* 2013).

Our derivation is consistent with ideas proposed initially by Tarantola & Valette (1982), who argued that modelling uncertainties can be incorporated into the inversion framework by adding a term to the data covariance matrix that represents the uncertainties in the physical theory (i.e. $\mathbf{C}_\mathrm{p}$). However, we differ from Tarantola & Valette (1982) by recognizing that our prediction covariance matrix $\mathbf{C}_\mathrm{p}$ should also depend on the earthquake source model and is not just a constant matrix, that is, changing the magnitude and distribution of fault slip will change $\mathbf{C}_\mathrm{p}$ for a given elastic model. For practical implementation, there are different ways of dealing with the dependence of $\mathbf{C}_\chi = \mathbf{C}_\mathrm{d} + \mathbf{C}_\mathrm{p}$ upon the source model $\mathbf{m}$. For example, one can calculate $\mathbf{C}_\mathrm{p}(\mathbf{m}_\mathrm{prior})$ using an *a priori* source model, $\mathbf{m}_\mathrm{prior}$, such as a centroid-moment-tensor solution or a preliminary finite-fault model and assume that $\mathbf{C}_\mathrm{p}$ is constant. In contrast, we propose here to update the prediction covariance during the

source inversion process. More precisely, in our implementation of CATMIP, the sample mean $\langle \mathbf{m} \rangle$ at each transitional step is used as a new model to re-compute $\mathbf{C}_\mathrm{p}$. Therefore, we assume that $\mathbf{C}_\mathrm{p}$ does not vary significantly in the neighbourhood of $\langle \mathbf{m} \rangle$, which ensure that the likelihood term $p(\mathbf{d}_\mathrm{obs}|\mathbf{m})$ in eq. (22) is Gaussian for a given value of β. For computational efficiency, the slip inversion being a linear problem $\mathbf{d} = \mathbf{G}\mathbf{m}$, we can pre-calculate the sensitivity kernels for each Green's functions in the matrix $\mathbf{G}$

$$(\mathbf{K}_\Omega^G)_{ijk} = \frac{\partial\, G_{ik}}{\partial \log \Omega_j}, \tag{23}$$

such that

$$\mathbf{K}_\Omega = \mathbf{K}_\Omega^G \cdot \langle \mathbf{m} \rangle. \tag{24}$$

In practice, this approach can be used for static and seismic data.

Although $\mathbf{K}_\Omega^G$ can be pre-computed, its calculation remains a challenging problem. We propose here to use the perturbation theory which has been extensively employed in seismic tomography through the Born approximation (e.g. Marquering *et al.* 1998; Tromp *et al.* 2005; Virieux & Operto 2009) and has been introduced for quasi-static problems by Du *et al.* (1994) and Cervelli *et al.* (2002). In the motivational example presented in Section 4, we use analytical solutions that are available in the quasi-static case for infinite strike-slip faults embedded in a layered earth model (Du *et al.* 1994). For non-infinite faults, one can increase the efficiency of the sensitivity kernel calculation by adopting an adjoint formulation. This approach allows a reduction in the computational cost when the number of stations is small compared to the number of elements and is popular in various fields such as 3-D seismic tomography (Tarantola 1984, 1988; Tromp *et al.* 2005), inverse problems in elasticity (Bonnet & Constantinescu 2005) and meteorological studies (Talagrand & Courtier 2007). To further increase the computational tractability of the sensitivity kernel calculations, we can also consider a limited number of tectonically parametrized regions where the uncertainties on elastic parameters are prescribed. Indeed, we are not interested in assigning variable uncertainties on a fine mesh but rather describing the earth model uncertainty in a limited number of tectonic regions (e.g. crust, mantle, etc.).

4 APPLICATION TO GEODETIC DATA: A MOTIVATIONAL EXAMPLE

In this synthetic application, we study the static surface displacements due to a vertical strike-slip fault and solve for the depth distribution of slip given uncertainties in the depth distribution of shear modulus (μ) in the elastic medium. With this purpose, we consider a simple model of an infinite 2-D strike-slip fault embedded in a shallow low compliance layer of thickness H overlying an elastic half-space (*cf.* red line on Figs 2b and d). We define μ_2, the shear modulus in the half-space and μ_1, the shear modulus in the shallow layer so that $\mu_2/\mu_1 = 1.4$. Given synthetic data at 100 observation points regularly sampled from the surface deformation of this 2-D model, we infer the depth distribution of slip assuming a homogeneous elastic half-space and accounting for the uncertainty in μ using the formulation of $\mathbf{C}_\mathrm{p}$ described in Section 3.2. For simplicity, we assume no uncertainty on the Poisson's ratio although this can easily be implemented using our formalism of $\mathbf{C}_\mathrm{p}$. The 2-D calculation of $\mathbf{C}_\mathrm{p}$, the fault parametrization as well as practical implications of using a non-constant prediction covariance structure are addressed in the following sections.

4.1 Calculation of $\mathbf{C}_\mathrm{p}$ in two dimensions

In this application example, we want to take into account the prediction error due to uncertainty in the 1-D shear modulus structure ($\boldsymbol{\Omega} = \boldsymbol{\mu}$). In this case, the prediction covariance $\mathbf{C}_\mathrm{p}$ defined in eq. (20) can be rewritten as

$$\mathbf{C}_\mathrm{p} = \mathbf{K}_\mu \cdot \mathbf{C}_\mu \cdot \mathbf{K}_\mu^T. \tag{25}$$

From this equation, we know that in order to obtain $\mathbf{C}_\mathrm{p}$, we need to estimate the shear modulus sensitivity kernel $\mathbf{K}_\mu$ and to choose an appropriate covariance $\mathbf{C}_\mu$ describing the uncertainty on $\boldsymbol{\mu}$. For practical implementation, we discretized the earth model into 50 small layers from depth of 0 to $5H$, where H is the thickness of the shallow layer. We then compute the sensitivity of the predictions with respect to the shear modulus in each layer using the first-order perturbations introduced initially by Du *et al.* (1994) for infinite strike-slip faults. The calculation of $\mathbf{K}_\mu$ in the quasi-static case is detailed in Appendix B.

In this simple implementation of $\mathbf{C}_\mathrm{p}$, the covariance matrix $\mathbf{C}_\mu$ is used to describe the uncertainty and correlations of the shear modulus for each of the 50 layers used to discretize the earth model. Various covariance structures in $\mathbf{C}_\mu$ can designed depending on the amount of information available about the earth model. Two different forms of $\mathbf{C}_\mu$ are presented in Figs 2(a) and (c). To illustrate the corresponding uncertainty on $\boldsymbol{\mu}$, Figs 2(b) and (d) show 1000 stochastic earth model realizations that are drawn for each form of $\mathbf{C}_\mu$ (*cf.* eq. 16). It should be noted that static predictions are only affected by gradients in elastic parameters and are not sensitive to absolute values in $\boldsymbol{\mu}$. Therefore, in this implementation, we take the half-space as the reference and allow the shear modulus to vary in the shallow layers. In Figs 2(a)–(b), we assume that the shallow layer thickness is known but that the shear modulus contrast with the homogeneous half-space is uncertain. In this case, we have a sharp transition in $\mathbf{C}_\mu$ between the shallow layer and the homogeneous half-space. In Figs 2(c)–(d), we consider the layer thickness as uncertain and we assume a smooth transition using a decaying exponential correlation function for depth larger than $0.8H$.

Figs 3(a) and (c) show the corresponding covariance matrices $\mathbf{C}_\mathrm{p}$ obtained for a simple uniform unit slip distribution between 0 to $0.9H$ where H is the thickness of the shallow layer. Figs 3(b) and (d) present 1000 stochastic prediction realizations for both versions of $\mathbf{C}_\mathrm{p}$. Note that $\mathbf{C}_\mathrm{p}$ is not very different for the two forms of $\mathbf{C}_\mu$, even though the prediction uncertainty for distant stations is slightly larger if we include uncertainty in the layer thickness. Several interesting features can be identified in the prediction covariance matrix structure. From the diagonal elements of $\mathbf{C}_\mathrm{p}$, we note first an increase of the prediction uncertainty as one approaches the fault, in agreement with the idea proposed by Minson *et al.* (2013) that mismodelling error should be roughly proportional to the data amplitude. However, we also note a drop of prediction uncertainty for observation points very close to the fault, since they provide direct slip measurements that have little sensitivity to the shear modulus. The off-diagonal covariance components show a clear anticorrelation with values on the opposite side of the fault for the form of $\mathbf{C}_\mu$ considered here. If the predicted data happen to be anomalously large on one side, the prediction must also be anomalously large but of opposite sign on the other side of the fault. The prediction covariance $\mathbf{C}_\mathrm{p}$ thus provides essential information about data weighting and data correlation that should be taken into account in the inverse problem.

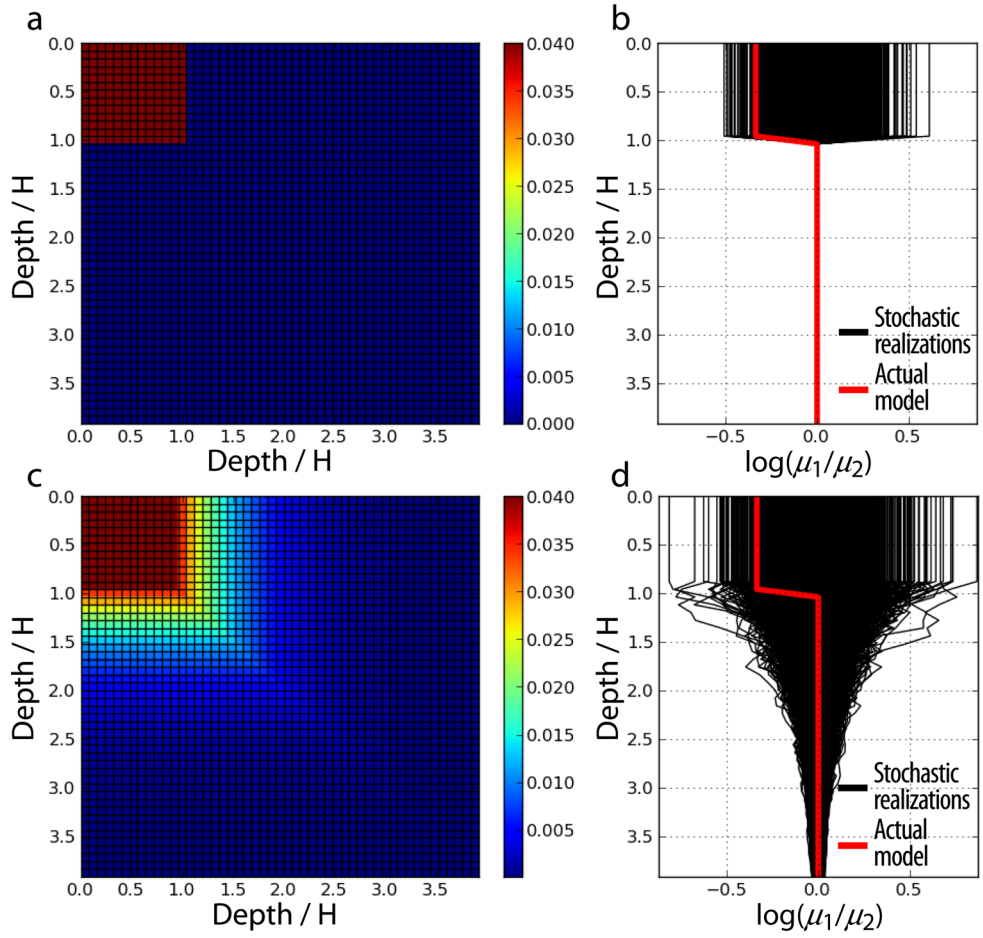

Figure 2. Uncertainty in the 1-D shear modulus structure $\boldsymbol{\mu}$. The shear modulus uncertainty is presented in (a)–(b) assuming a fixed thickness H for the shallow layer and in (c)–(d) considering the layer thickness as uncertain. For both cases, we present the shear modulus covariance matrix $\mathbf{C}_\mu$ in (a) and (c). Using eq. (16) to sample for each form of $\mathbf{C}_\mu$, we show 1000 stochastic earth model realizations in (b) and (d), where individual stochastic realizations are plotted in black and the actual earth model is presented in red. We define μ_1, the shear modulus in the shallow layers and μ_2, the shear modulus in the half-space.

4.2 A side comment on fault parametrization

In this section, we investigate the model resolution in order to design a proper parametrization of the fault. We aim to derive a fault discretization that allows us to accurately reflect the slip distribution and account for the resolving power of available measurements. Furthermore, to allow a natural comparison between the inferred model and the true slip distribution, we need to understand the fundamental spatial resolution of the estimated slip model.

Fig. 4 shows the inversion results obtained for a target slip distribution with 1-m uniform slip (i.e. $\mathbf{m} = 1$ m) at depths between 0 and $0.9H$. We use $p(\mathbf{m}) = \mathcal{U}(-0.3, 20)^M$ as the prior information on the slip parameters $\mathbf{m}$ (i.e. a uniform probability distribution from -0.3 to 20 m in M-dimensions). As described above, the data computed for a layered half-space with $\mu_2/\mu_1 = 1.4$ (*cf.* red line in Fig. 2 d) is inverted using Green's functions for a homogeneous half-space including our formulation of $\mathbf{C}_\mathrm{p}$ (using the shear modulus structure $\mathbf{C}_\mu$ shown in Fig. 2c). The results obtained if we neglect $\mathbf{C}_\mathrm{p}$ are presented in Fig. S1 of the Supporting Information and the advantages of including $\mathbf{C}_\mathrm{p}$ in the inversion are discussed latter (see Section 4.3).

Histograms in Fig. 4(a) present the marginal PDFs obtained if the fault is discretized into 16 fault patches. Apart for the shallowest subfault, the shape of these marginals clearly suggests a multivariate Dirichlet distribution of slip over group of adjacent patches. An N_p-dimensional Dirichlet distribution produces sets of N_p stochastic positive numbers that sum to a given constrained value (*cf.* Minson *et al.* 2013). The marginal of a Dirichlet distribution is a beta distribution of the form

$$\beta(m_i|1, N_p - 1) \propto (1 - m_i)^{N_p - 2}, \tag{26}$$

where we assumed unit concentration parameters (Bishop 2006). The best-fitting Beta distributions shown in black in Fig. 4(a) indicate that optimum values for N_p range between 2 and 4. This suggests that the sum of slip on $N_p \sim 3$ neighbouring patches can be resolved while it is poorly constrained on individual subfaults. Fig. 5 shows some model samples chosen randomly near the mean of the posterior distribution. For these models, the distribution of slip shows strong oscillations over adjacent patches while the average slip over group of subfaults are consistent with the target model. The best-fitting Dirichlet distributions along with this checker-boarding of neighbouring subfaults indicate that the slip can be well resolved over $N_p \sim 3$ neighbouring patches, that is, at a scale of about $0.2H$. Histograms in Fig. 4(b) present marginal PDFs similar to Fig. 4(a) with the fault discretized into 32 fault patches. In this case, the best-fitting Dirichlet distribution indicates checkerboarding over $N_p \sim 6$ patches which corresponds to a resolution scale of about $0.2H$, consistent with results obtained using the 16 patches discretization.

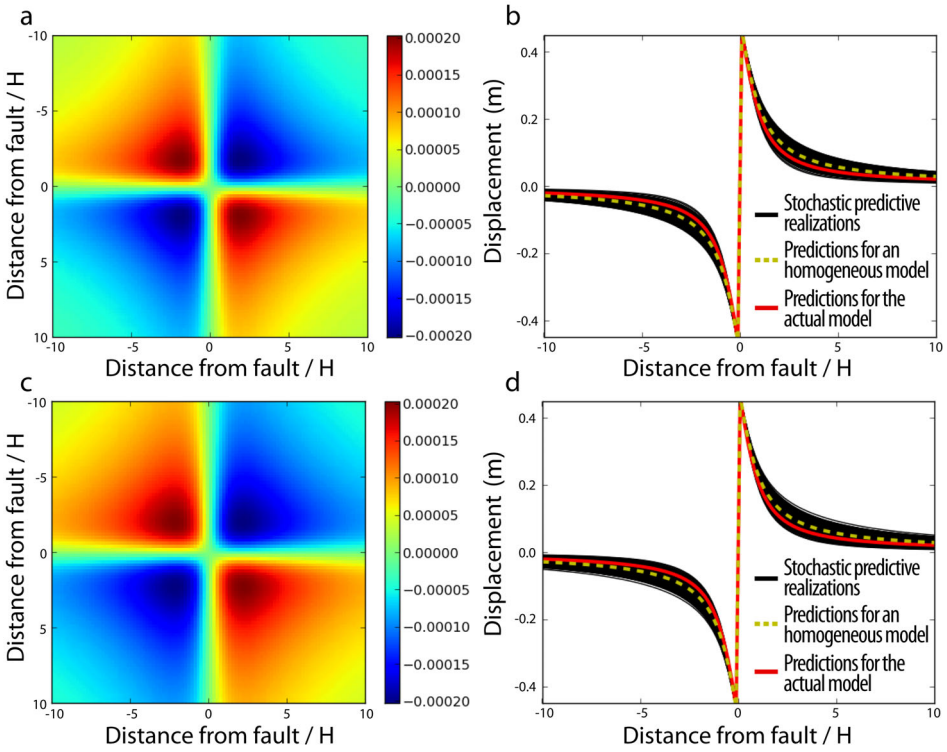

Figure 3. Prediction uncertainty in a 2-D quasi-static case. We assume a simple infinite strike-slip fault with unit slip from the free surface to $0.9H$, where H is the thickness of the shallow layer (*cf.* red line in Fig. 2). Panels (a) and (b) illustrate the prediction uncertainty statistics if we assume a fixed thickness for the shallow layer (*cf.* Figs 2a–b). Panels (c) and (d) present the predictive stochastic model obtained if we consider some uncertainty on the layer thickness (*cf.* Figs 2c–d). For both cases, we present the corresponding prediction covariance matrices in (a) and (c). For each stochastic model, we show 1000 stochastic predictions in (b) and (d) in black assuming a homogeneous half-space. The predicted data for the actual layered earth model is shown in red and the predictions for a homogeneous half-space are shown as yellow dashed lines.

There are several different possibilities to take into account this limited resolution. A first possibility is to increase the size of patches, therefore using a coarse fault discretization. This possibility has already been explored by Pritchard *et al.* (2002) and Barnhart & Lohman (2010) who proposed to use variable patch sizes depending on the resolution scale on the fault. On the other hand, one should assign small patch sizes to enhance the accuracy of the forward modelling in order to minimize parametrization errors due to the assumption of constant slip on elements that produces sharp discontinuities. A better practice is thus to use a discretization smaller than the actual resolution scale and eventually to filter the slip distribution *a posteriori* using a smoothing or averaging length comparable to the resolution scale. Therefore, we prefer here to use 16 fault patches and to account for the model resolution scale using local averaging rather than using coarse discretization. Fig. 4(c) shows marginal distributions of filtered model samples using an arithmetic mean over a sliding window of $N_p = 3$ patches. These results show a Gaussian-like distributions that are well centred around the target slip value (i.e. $\mathbf{m} = 1$ m), which confirms the possibility to resolve slip over three to four patches.

4.3 Comparison of inversion results with and without neglecting the prediction uncertainty

To assess the impact of including $\mathbf{C}_\mathrm{p}$ in the estimation process, we compare inversion results with and without neglecting the prediction uncertainty. We assume a non-uniform target slip distribution from 0 to $0.9H$ presented in Fig. 6(a). We compute the data for the layered half-space presented in red in Fig 2(d) and add 5 mm of uncorrelated Gaussian observational noise. The resulting data vector is presented in red in Figs 6(d)–(f). Once again, the source inversion is performed assuming a homogeneous half-space. We therefore include the two classes of errors discussed in Section 2—errors on the measurements and in the predictions. As described before, we use a simple uniform prior $p(\mathbf{m}) = \mathcal{U}(-0.3, 20)^M$ on the slip distribution, a fault discretized into 16 patches, and a smoothing window over three patches. The measurement covariance matrix $\mathbf{C}_\mathrm{d}$ is diagonal with standard deviation of 5 mm. For the calculation of $\mathbf{C}_\mathrm{p}$, we consider the first layer thickness as uncertain (i.e. $\mathbf{C}_\mu$ in Fig. 2c) and use a prediction covariance structure similar to the one presented in Fig. 2.

The comparison of the posterior model distribution mean with and without neglecting the prediction uncertainty are shown, respectively, on Figs 6(b) and (c). The corresponding 1-D and 2-D marginal posterior PDFs for each fault patch are also presented in Fig. 7 [each $p(m_i|\mathbf{d}_\mathrm{obs})$] and Fig. 8 [each $p(m_i, m_j|\mathbf{d}_\mathrm{obs})$] based on nearly 700 000 samples of the slip vector $\mathbf{m}$. We note significant discrepancies in the inversion results depending on whether the prediction covariance matrix $\mathbf{C}_\mathrm{p}$ is included or ignored. If $\mathbf{C}_\mathrm{p}$ is neglected, the mean of the distribution shown in Fig. 6(b) is very different from the target model in Fig. 6(a). Estimated slip values are larger than the target model for depths between 0.2 and $0.4H$ and significantly lower than the target slip value at larger depth. We note also that the uncertainty on the slip distribution is clearly underestimated: the marginal PDFs in Figs 7(a) and 8(lower left) show very narrow peaks at large depth that are clearly shifted with respect to the target slip values. On the other hand, if $\mathbf{C}_\mathrm{p}$ is included, we

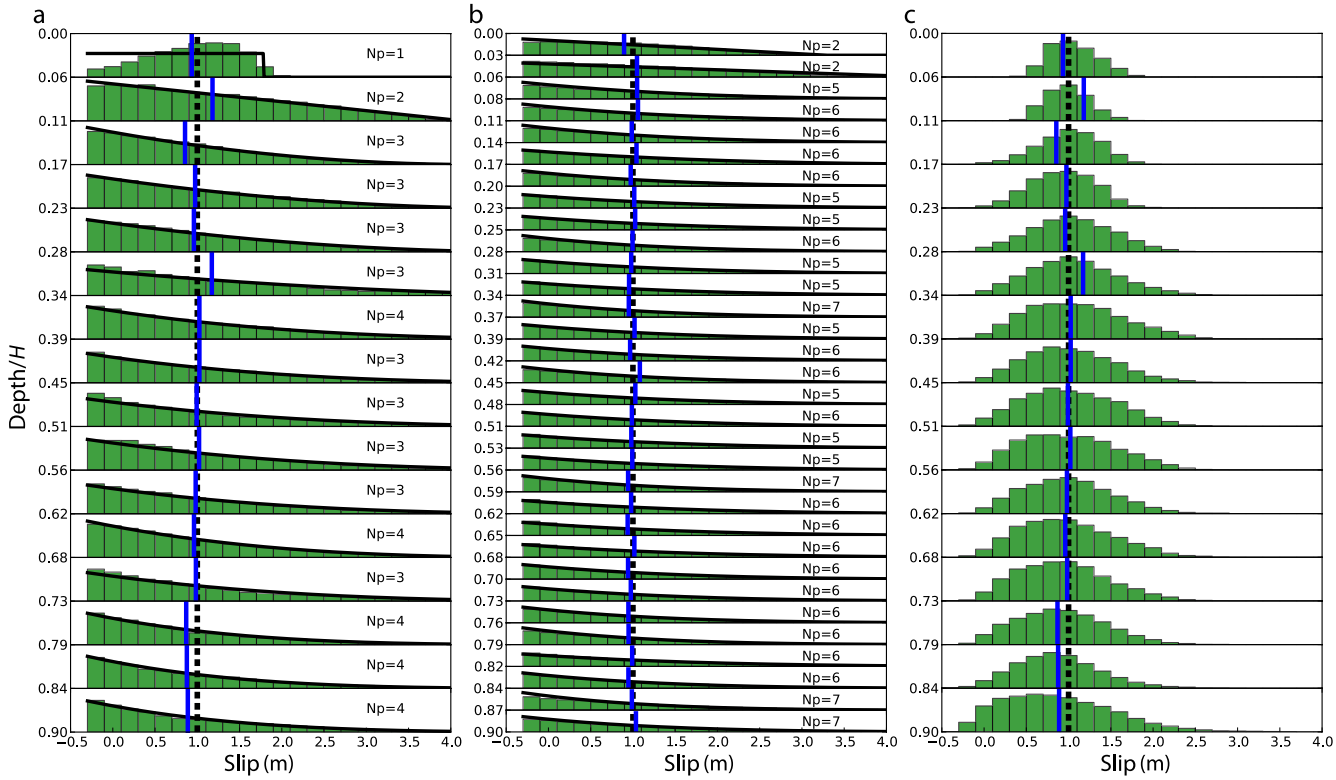

Figure 4. Source estimation for a constant unit slip distribution. Raw marginal PDFs for the slip in each fault patch are shown in (a) if the fault is discretized into 16 patches and in (b) if the fault is discretized into 32 patches. The target slip model is indicated as dashed black lines and the mean of the distribution is shown in blue. The number of parameters N_p of the best-fitting marginal Dirichlet distribution (black curves) is indicated for each patch. The marginal PDFs for 16 patches after using a moving average over three neighbouring patches is shown in (c).

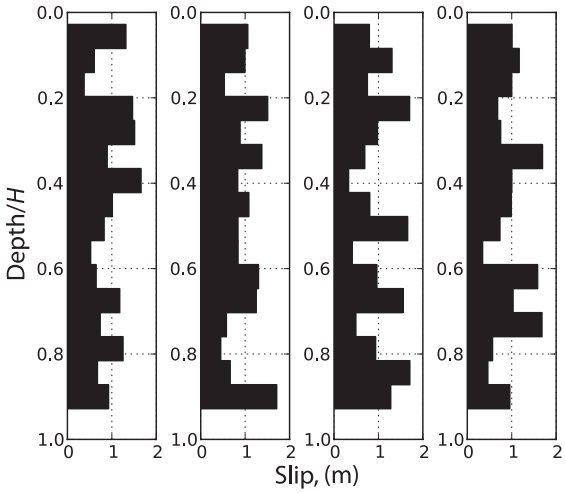

Figure 5. Examples of model samples chosen near the mean of the posterior distribution. The fault from 0 to 0.9H is discretized into 16 fault patches. The depicted models are the four samples closest to the mean of the posterior distribution in a CATMIP simulation of 8192 samples.

obtain much broader posterior distributions centred around a mean model that is in agreement with the target slip model. This increase of estimated posterior uncertainty is particularly visible on the 2-D marginal posterior PDFs in Fig. 8. In this figure, we also note a slight correlation between neighbouring patches at large depth (i.e. for patches P 5–P 16), which is certainly related to the averaging of slip on neighbouring patches as described in the previous section. This correlation among adjacent patches will not affect inversion results as long as the slip distribution is relatively smooth as in Fig. 6(a). It can however be problematic if the target model includes short-scale variations of slip. To explore this possibility, Fig. 9 shows inversion results for a target model including an abrupt drop of 1 m in the slip distribution at depth 0.56H (*cf.* dashed black lines). As in the case of the smoother slip model in Fig. 7 , the introduction of $\mathbf{C}_\mathrm{p}$ significantly improves the posterior model estimates. However, in Fig. 9(b), we note that the mean model (blue lines) is relatively smooth and does not reproduce the slip step at a depth of 0.56H. The step in slip cannot be recovered because in this example we can only resolve features over a scale corresponding to three neighbouring patches (*cf.* Section 4.2). Consequently, the mean model shows better agreement with the filtered target model shown in white in Fig. 9(b), which corresponds to a three-neighbouring-patches moving average of the initial target model. In any case, note that both raw and filtered target models are within the error bounds defined by the posterior marginal distribution histograms. The two simple models presented here clearly illustrate the importance of using an accurate stochastic model for the prediction uncertainty in order to reliably infer the posterior distribution of source model parameters. Using our formulation for $\mathbf{C}_\mathrm{p}$, we can obtain more realistic estimates of the posterior uncertainty but also improve the slip distribution model.

4.4 Dependence of prediction uncertainty upon the source model

An important finding of this work is the dependence of the prediction error upon the source model parameters **m**. Two critical questions

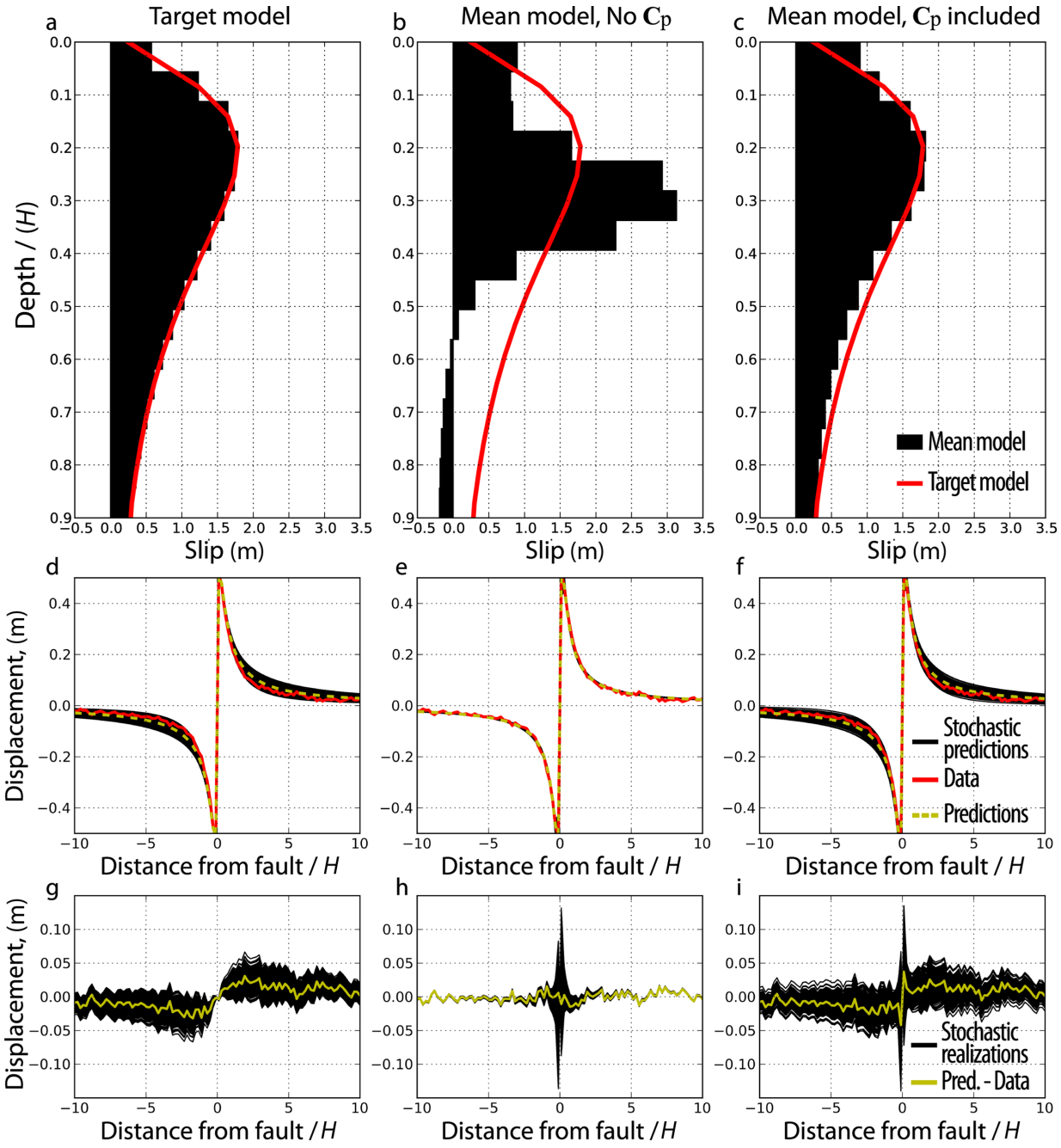

Figure 6. Comparison of inversion results with and without neglecting the prediction uncertainty. Panel (a) is the target slip model. The mean of the posterior distributions are shown in black (b) when the prediction uncertainty is neglected and (c) when $\mathbf{C}_p$ is included in the estimation process. The continuous red line corresponds to the target slip model. Comparisons between data and predictions for each model in a homogeneous half-space are shown in (d)–(f). The data are presented in red. The predictions shown in yellow are calculated for each model presented in black in (a)–(c). Black lines correspond to a set of 1000 stochastic realizations drawn from the posterior predictive PDF defined in eq. (27). The residuals between data and predictions are shown in (g)–(i). The yellow line is the difference between the data and the predictions presented, respectively, in red and yellow in (d)–(f). Black lines are the residuals between data and the 1000 stochastic predictions shown in (d)–(f).

need to be addressed. First, how is it possible to account for the coupling between $\mathbf{C}_p$ and the source model? Secondly, what is the variation of $\mathbf{C}_p$ as a function of $\mathbf{m}$?

As discussed in Section 3.3, we propose here to account for the coupling between $\mathbf{C}_p$ and $\mathbf{m}$ by updating the covariance at each transitional step (i.e. increase of β in eq. 22) using the mean of the model distribution. The prediction uncertainty covariance matrix $\mathbf{C}_p$ is therefore considered here as a by-product of the inversion. We explored different possibilities to design $\mathbf{C}_p$ at $\beta_0 = 0$: (1) calculating $\mathbf{C}_p$ from the mean of the distribution $\langle \mathbf{m} \rangle$ at $\beta_0 = 0$, (2) computing $\mathbf{C}_p$ for a uniform unitary slip distribution as a function of depth, (3) calculating $\mathbf{C}_p$ from the solution of a prior source

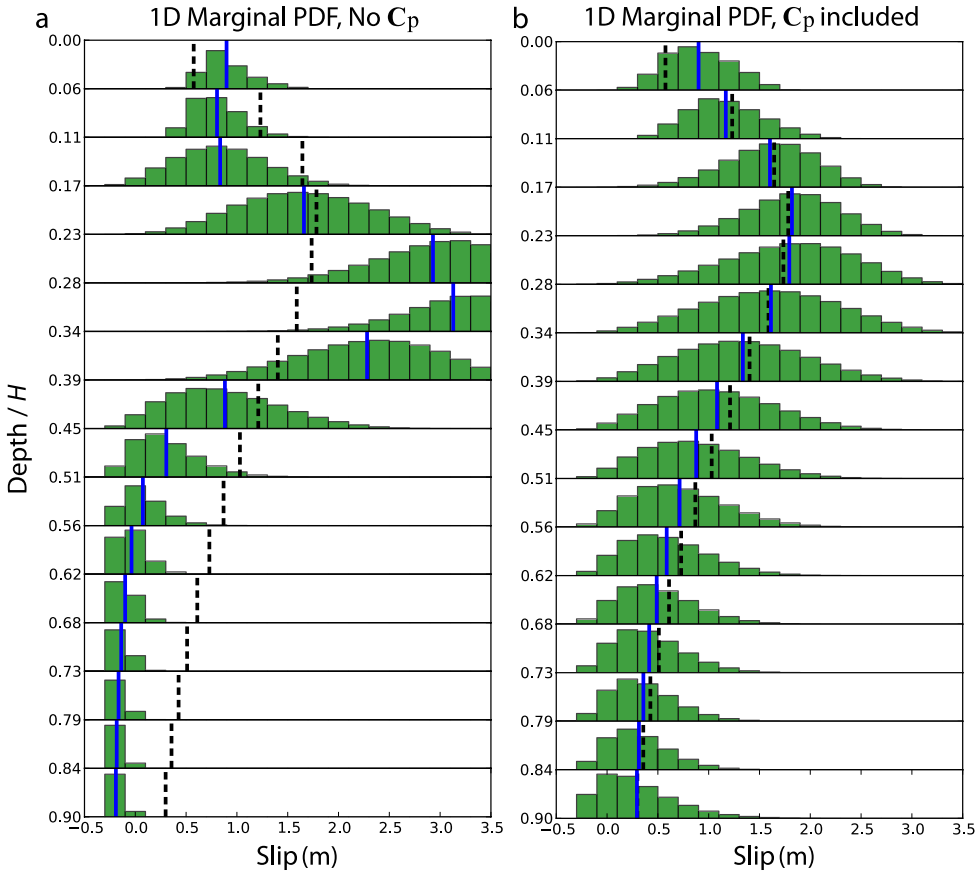

Figure 7. 1-D marginal posterior PDFs for each patch as a function of depth. The marginal probability density histograms are shown in green (a) when the prediction uncertainty is neglected and (b) when the prediction uncertainty is taken into account by including $\mathbf{C}_\mathrm{p}$ in the inversion problem. The target slip model is indicated as dashed black lines and the mean of the distribution is shown in blue.

inversion in which $\mathbf{C}_\mathrm{p}$ is neglected and (4) using a preliminary form of $\mathbf{C}_\mathrm{p}$ whose diagonal elements are proportional to the observations as suggested by Minson *et al.* (2014). Fig. 10 presents the evolution of the prediction covariance in the sampling process using the mean of the distribution $\langle \mathbf{m} \rangle$ at $\beta_0 = 0$ (*cf.* Fig. 11). This evolution of $\mathbf{C}_\mathrm{p}$ corresponds to the estimation process for the target model presented in Figs 6–8. Similar figures using approaches (2), (3) and (4) are shown in Figs S2–S10. For all four cases, we note that $\mathbf{C}_\mathrm{p}$ converges properly to the covariance structure estimated from the target model and that the posterior distributions are almost identical. Less transitional steps are however necessary when using a diagonal $\mathbf{C}_\mathrm{p}$ proportional to the observations at $\beta_0 = 0$ (*cf.* Figs S9 and S10).

The mean models used to compute $\mathbf{C}_\mathrm{p}$ are presented in Fig. 11. The transitional process is clearly illustrated by the evolution of the model sample mean shown in this figure. The mean models at the first few transitional steps are largely controlled by the prior PDF [i.e. uniform probability distribution $p(\mathbf{m}) = \mathcal{U}(-0.3, 20)^M$] and then slowly converge to the target model as more weight is given to the likelihood (i.e. as β increases). The corresponding covariance matrix structures do not change significantly at each update although the overall magnitude of $\mathbf{C}_\mathrm{p}$ is quite different for small and large values of β. Note that an additional sampling step is performed after reaching $\beta = 1$ in order to resample the posterior PDF with a prediction covariance estimated from the sample mean at $\beta_B = 1$. However, only minor differences are visible after the final update of $\mathbf{C}_\mathrm{p}$.

5 DISCUSSION

The previous synthetic application clearly illustrates the importance of incorporating inaccuracies of the earth model in the prediction uncertainty in source estimation problems. When neglecting $\mathbf{C}_\mathrm{p}$, the posterior mean model shows strong oscillations with a slip distribution that is overestimated between 0.2 and 0.4H and underestimated at larger depth. We observe similar features for a constant unit slip distribution in Fig. S1(b). Note that the negative slip at larger depth is due to the lower bound of the prior distribution $p(\mathbf{m}) = \mathcal{U}(-0.3, 20)^M$ used to obtain these results. Using strictly positive constraints leads to similar slip distributions as shown in Fig. S11. These oscillatory artefacts when $\mathbf{C}_\mathrm{p}$ is neglected are clearly related to errors in the Green's functions that are calculated for an homogeneous half-space instead of a layered medium. To explain these artefacts, Fig. 12 shows the result of a simple linear least-square inversion without positivity constraints (i.e. a purely Gaussian case without prior information). In this example, we consider noise-free data but still use incorrect Green's functions (i.e. assuming an homogeneous half-space instead of the actual layered half-space with $\mu_2/\mu_1 = 1.4$). As shown in Fig. 12(a), if we assume shallow slip on a fault with large a depth extent, the inferred least-squares solution has strong artefacts at depth due to inaccuracies in the predictions based on a homogeneous elastic half-space. The model including $\mathbf{C}_\mathrm{p}$ in Fig. 12(b) shows similar artefacts but has error bars indicating that deep slip cannot be resolved given the uncertainty in μ. The inferred slip model is actually identical to

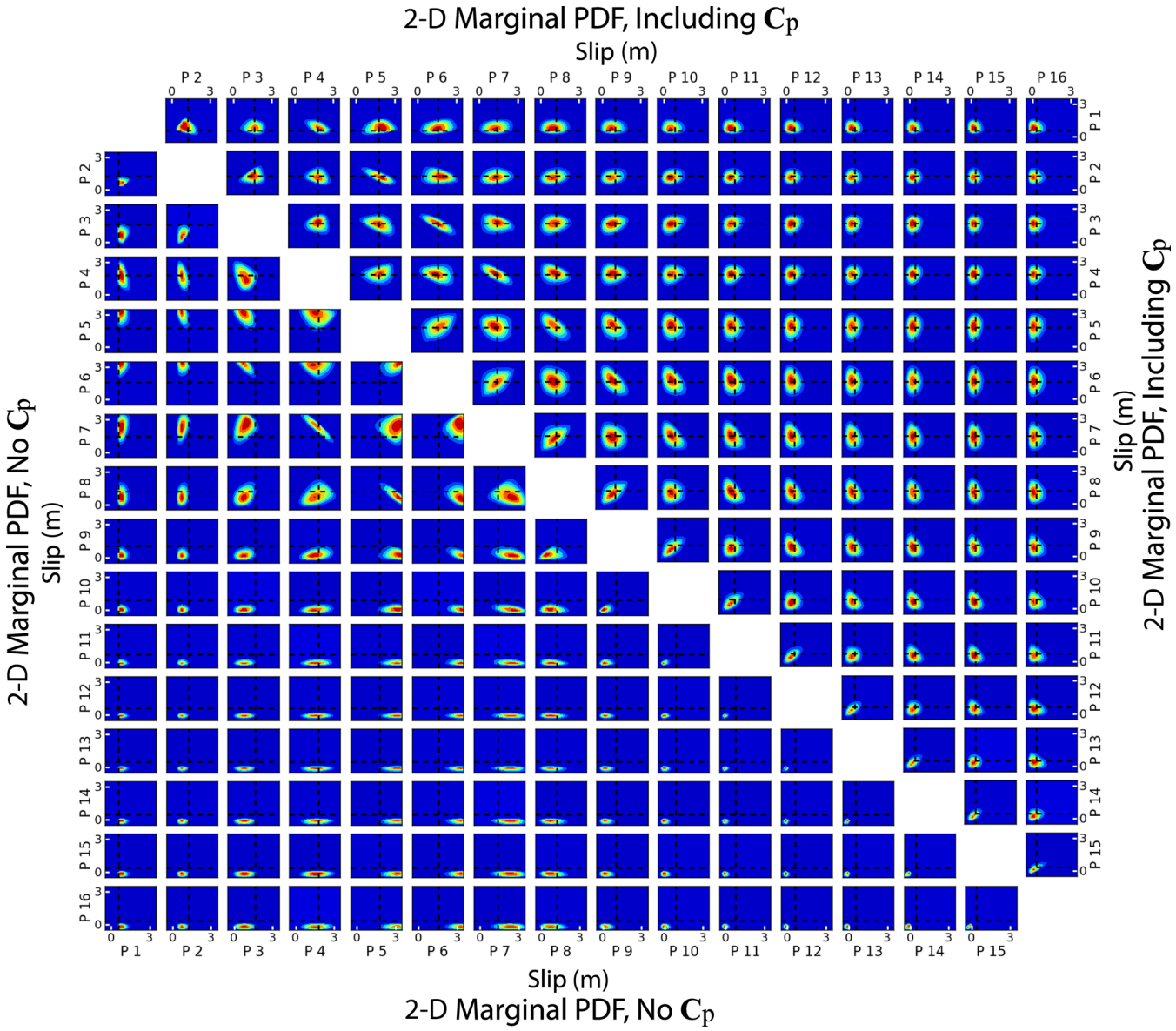

Figure 8. 2-D marginal posterior probability densities for all possible pairs of fault patches. Fault patches are numbered increasingly as a function of depth (e.g. P 16 is the deepest fault patch). The 2-D histograms are shown (bottom left) when $\mathbf{C}_p$ is neglected and (top right) when the prediction uncertainty is accounted for. Dashed black lines indicate the target slip value for each fault patch.

the series of dislocations derived by Savage (1987) and presented in Fig. 12(c). This slip distribution produces surface displacements that are exactly identical to the input target slip model in a layered half-space. Of course, in common source inversion practices, faults are parametrized with a limited depth extent and the prediction error cannot be perfectly mapped in the distribution of slip. Fig. 13 illustrates such case with a constant target slip model discretized in four slices down to $0.9H$. We note strong oscillations when $\mathbf{C}_p$ is neglected. Although there is no obvious analytical solution such as Savage (1987) in this case, these oscillations are clearly due to inaccuracies of half-space predictions since this is the only source of uncertainty considered here. On the other hand, the model including $\mathbf{C}_p$ is able to properly resolve the input target model since error in the Green's function cannot be perfectly reproduced by slip oscillations.

To get more insight on the improvement of inversion results using our formulation of $\mathbf{C}_p$, we propose here to estimate the posterior prediction uncertainty for the simple model presented in Fig. 6. To do so, we calculate the posterior predictive distribution $p(\mathbf{d}|\mathbf{d}_{obs})$ using the stochastic forward model $p(\mathbf{d}|\mathbf{m})$ in eq. (4) and the posterior model distribution $p(\mathbf{m}|\mathbf{d}_{obs})$ in eq. (8):

$$p(\mathbf{d}|\mathbf{d}_{obs}) = \int_{\mathfrak{M}} p(\mathbf{d}|\mathbf{m})\, p(\mathbf{m}|\mathbf{d}_{obs})\, \mathrm{d}\mathbf{m}. \quad (27)$$

This equation can be obtained directly from the total probability theorem (e.g. Bishop 2006) and describes the posterior variability on the predictions $\mathbf{d}$ due to modelling error [i.e. $p(\mathbf{d}|\mathbf{m})$] and posterior uncertainty on the slip distribution [i.e. $p(\mathbf{m}|\mathbf{d}_{obs})$]. The PDF $p(\mathbf{d}|\mathbf{d}_{obs})$ can also be seen as the posterior information on the displacement field. This posterior predictive PDF is illustrated in black in Figs 6(e)–(f) by showing 1000 stochastic realizations drawn from $p(\mathbf{d}|\mathbf{d}_{obs})$. In Figs 6(h)–(i), we show the corresponding residuals after subtracting the data vector from each predictive realization. For comparison, Figs 6(d) and (g) also show the posterior predictive

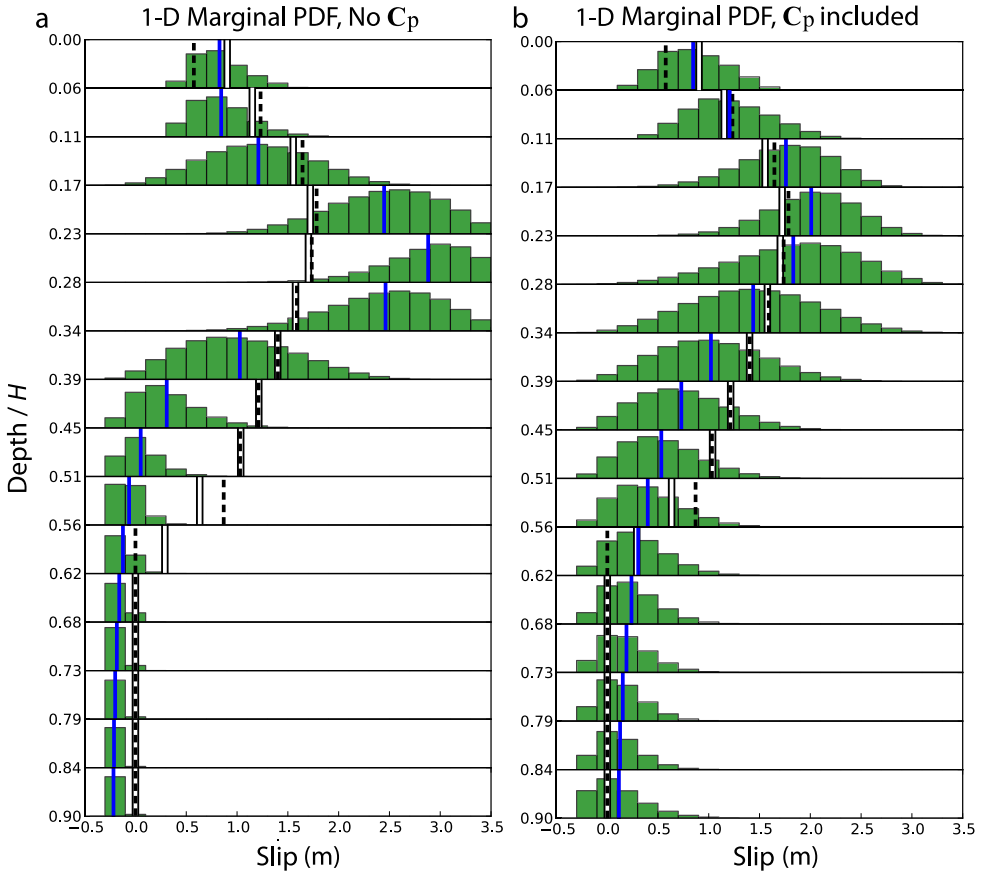

Figure 9. 1-D marginal posterior PDFs for a target model including a slip step of 1 m at 0.56*H*. The marginal probability density histograms are shown in green (a) when the prediction uncertainty is neglected and (b) when the prediction uncertainty is taken into account by including $\mathbf{C}_p$ in the inversion problem. The mean of the posterior model distribution is shown in blue. The raw target slip model is indicated as dashed black lines and the locally averaged target slip model using a moving window over three adjacent patches is shown in white.

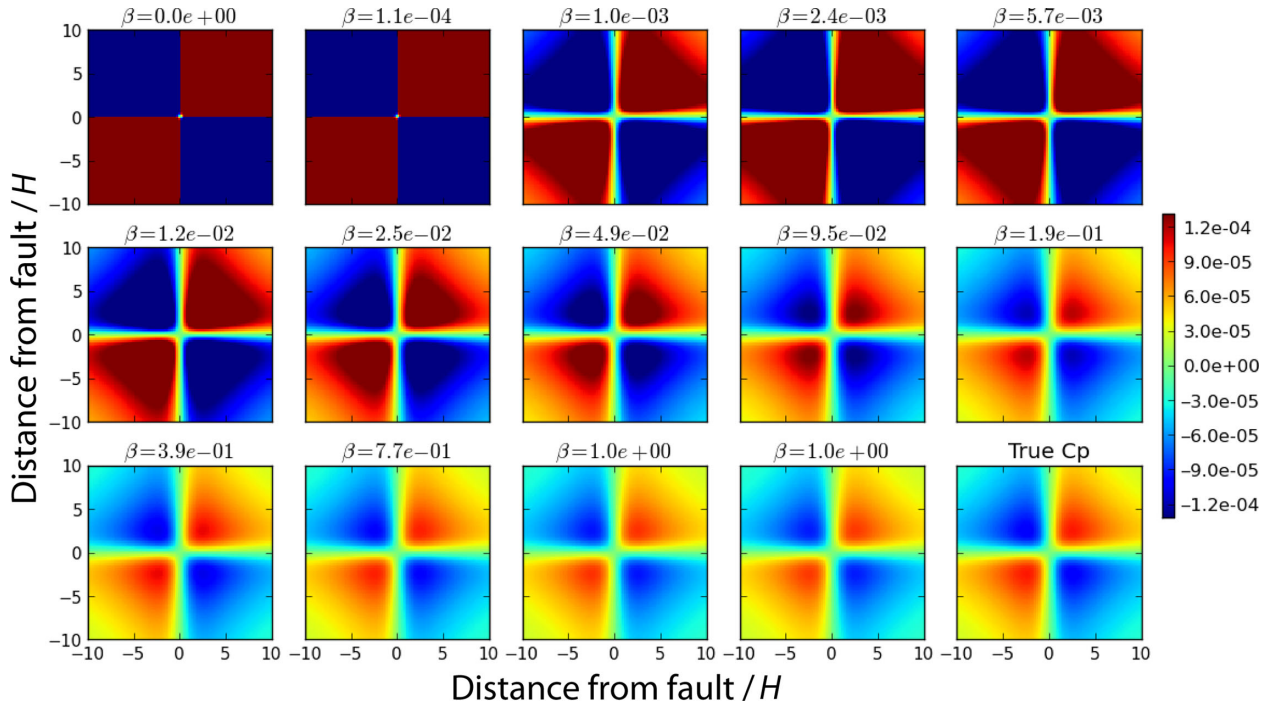

Figure 10. Evolution of the prediction covariance $\mathbf{C}_p$ at each transitional step. The values of β in eq. (22) are specified on top of each subfigure.

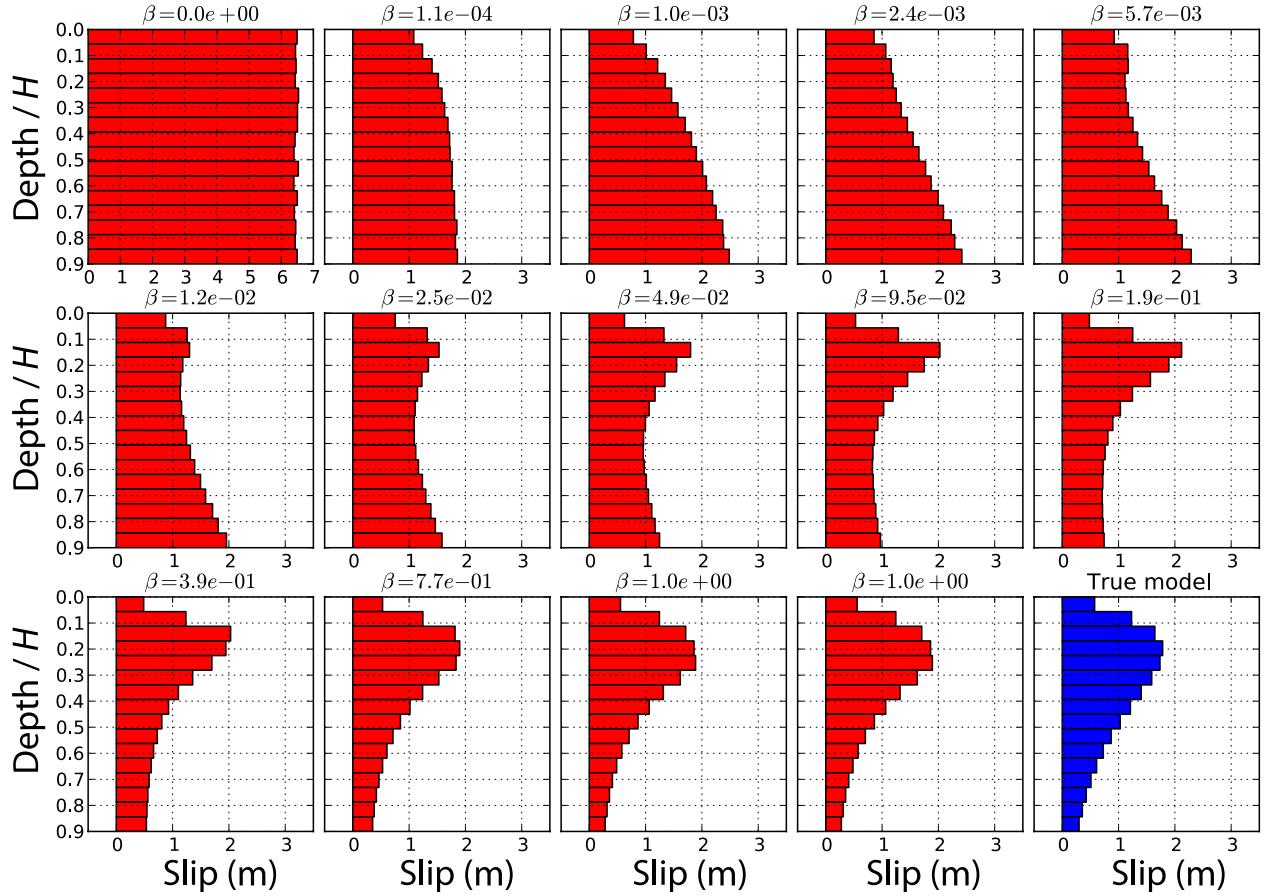

Figure 11. Slip models used for the calculation of the prediction covariance matrix $\mathbf{C}_p$. These slip models correspond to the mean of the model sample distributions at each transitional step. The values of β in eq. (22) are specified on top of each subfigures.

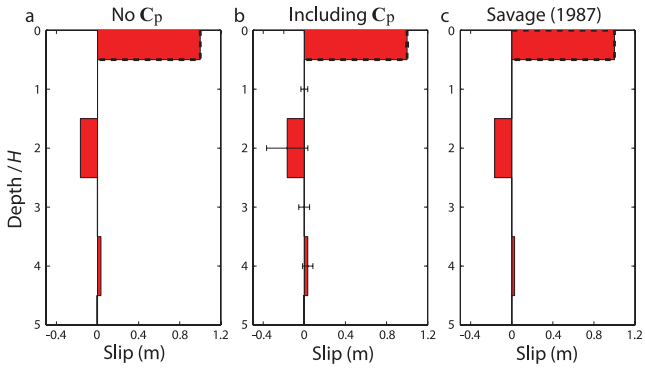

Figure 12. An illustration of the effects of prediction uncertainty on inversion results for an extend fault at depth. The target slip model, indicated as dashed black lines, is used to generate noise-free data in a layered half-space. Simple least-square inversion results for an extended fault in a homogeneous half-space are presented in (a) when $\mathbf{C}_p$ is neglected and (b) when $\mathbf{C}_p$ is included in the inversion. The calculation of $\mathbf{C}_p$ used in (b) is based on the maximum *a posteriori* (MAP) slip model shown in (a). These two MAP models are very similar to the theoretically derived half-space equivalent slip distribution by Savage (1987) presented in (c).

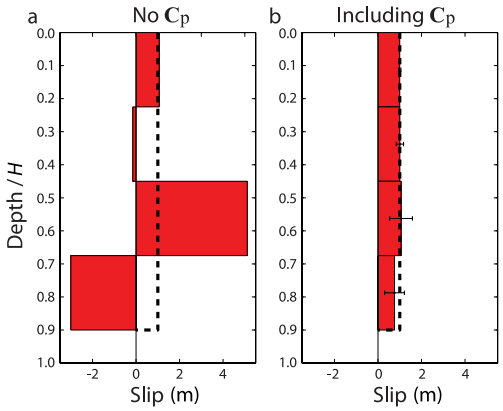

Figure 13. An illustration of the importance of the prediction covariance $\mathbf{C}_p$. The target slip model, indicated as dashed black lines, is used to generate noise-free data in a layered half-space. Simple least-square inversion results for an extended fault in a homogeneous half-space are presented in (a) when $\mathbf{C}_p$ is neglected and (b) when $\mathbf{C}_p$ is included in the inversion. The calculation of $\mathbf{C}_p$ used in (b) is based on the maximum *a posteriori* slip model shown in (a).

PDF for the target slip model, assuming no uncertainty on the slip distribution (i.e. $p(\mathbf{m}|\mathbf{d}_{obs}) = \delta(\mathbf{m} - \mathbf{m}_{true})$ where $\mathbf{m}_{true}$ is the target model). Figs 6(e) and (h) show the data fit if the prediction uncertainty is neglected [i.e. $p(\mathbf{d}|\mathbf{m}) = \delta(\mathbf{d} - \mathbf{g}(\mathbf{m}))$, where $\mathbf{g}(\mathbf{m})$ are the predictions for a homogeneous half-space]. In Figs 6(f) and (i), we use the stochastic forward model based on $\mathbf{C}_p$ for the same $\mathbf{g}(\mathbf{m})$ (i.e. $p(\mathbf{d}|\mathbf{m}) = \mathcal{N}[\mathbf{d}|\mathbf{g}(\mathbf{m}), \mathbf{C}_p]$). The posterior predictive uncertainty is significantly larger if $\mathbf{C}_p$ is taken into account. Even if the posterior variability of the source model is incorporated when $\mathbf{C}_p$ is neglected, we note that the posterior predictive uncertainty is negligible

compared to the variability when $\mathbf{C}_\mathrm{p}$ is included. Moreover, when comparing data with predictions for a homogeneous half-space, the data misfit is clearly smaller if the prediction uncertainty is neglected. This small data residual is due to data overfitting resulting from the use of a deterministic forward model. By neglecting $\mathbf{C}_\mathrm{p}$, too much information is conferred to imperfect forward predictions, leading to spurious posterior distributions which favour source models that closely explain observations. The differences between inversion results in Fig. 6(b) and the target model in Fig. 6(a) are thus certainly due to overfitting of observations using predictions for an inaccurate earth model (i.e. a homogeneous half-space instead of a layered medium). On the other hand, using a stochastic forward problem, we gain an extra flexibility by allowing some variability in the predictions, which allows us to select models having larger and correlated data residuals. Thus, the impact of including the prediction covariance $\mathbf{C}_\mathrm{p}$ is not just a better analysis of the posterior uncertainty. In fact, the use of $\mathbf{C}_\mathrm{p}$ also improves source parameter estimates by using physically based relative weights between measurements and by preventing overfitting of observations.

In this study, we have mainly focused on the impact of inaccuracies in the earth model, which significantly contribute to forward modelling errors. We recognize, however, that other contributors can have profound impact on the predictions. In particular, we know that approximation of the true source geometry by a fault surface $\widetilde{\boldsymbol{\phi}}$ based on prior information can be a major source of uncertainty in source estimation problems. A judicious approach is to incorporate $\boldsymbol{\phi}$ into the source model parameters $\mathbf{m}$ for which the data are inverted. However, this approach may be difficult to implement in practice since we would have to recalculate the Green's functions for each explored model, a computationally challenging prospect. Alternatively, if the imperfect fault surface is not grossly wrong, we can use our formulation of $\mathbf{C}_\mathrm{p}$ in order to account for the uncertainty in the fault geometry. One possibility is to design a $\mathbf{C}_\Omega$ that incorporates a high variability of elastic properties in a narrow zone around the fault. Another approach is to take into account a variability of $\boldsymbol{\phi}$ in the inversion problem. The latter possibility is formulated in the following.

Let us define a parameter $\boldsymbol{\Psi} = [\ln \boldsymbol{\Omega}^T, \boldsymbol{\phi}^T]^T$ incorporating all information about the earth model $\boldsymbol{\Omega}$ and fault surface $\boldsymbol{\phi}$ (which are assumed independent). As in Section 3.1, we assume that predictions $\mathbf{g}(\boldsymbol{\Psi}, \mathbf{m})$ are modelled as first-order perturbations of our predictions $\mathbf{g}(\widetilde{\boldsymbol{\Psi}}, \mathbf{m})$. In this case, the prediction covariance can be written as

$$\mathbf{C}_\mathrm{p} = \mathbf{K}_\Omega \cdot \mathbf{C}_\Omega \cdot \mathbf{K}_\Omega^T + \mathbf{K}_\phi \cdot \mathbf{C}_\phi \cdot \mathbf{K}_\phi^T. \tag{28}$$

The prediction uncertainty due to the fault geometry can therefore be included by augmenting the prediction covariance matrix with a new term $\mathbf{K}_\phi \cdot \mathbf{C}_\phi \cdot \mathbf{K}_\phi^T$, where $\mathbf{C}_\phi$ is the covariance matrix on fault geometry parameters and $\mathbf{K}_\phi(\widetilde{\boldsymbol{\Psi}}, \mathbf{m})$ is the corresponding sensitivity kernel

$$(\mathbf{K}_\phi)_{ij}(\widetilde{\boldsymbol{\Psi}}, \mathbf{m}) = \frac{\partial g_i}{\partial \phi_j}(\widetilde{\boldsymbol{\Psi}}, \mathbf{m}). \tag{29}$$

In this equation, the vector $\boldsymbol{\phi}$ can, for example, include averages of dip and strike values over the entire (or portions of) the fault. This approach can be extended to other sources of modelling uncertainty and we should be able to define a gallery of prediction covariance matrices to be included in the source inversion problem. However, this formulation is not appropriate if prediction uncertainties are too large since there will be no simple relationship between the corresponding predictions $\mathbf{g}(\widetilde{\boldsymbol{\Psi}}, \mathbf{m})$ and $\mathbf{g}(\boldsymbol{\Psi}, \mathbf{m})$. In such situations, the results of our inversion would be unreliable and more efforts should be spent to improve forward modelling capabilities. The ultimate goal would be to allow for updating the uncertainty in all model parameters (i.e. $\mathbf{m}$, $\boldsymbol{\Omega}$, $\boldsymbol{\phi}$) by sampling from their posterior PDF but this requires greatly increasing the computational speed for the forward modelling, either by computer hardware and/or faster algorithms (e.g. building surrogate (meta-) models of the forward model using machine learning methods; Bishop 2006).

6 CONCLUSION

This study improves the modelling of the misfit covariance matrix as used in inversions for the distribution of slip on subsurface faults. The misfit covariance, $\mathbf{C}_\chi$, is a combination of the observational covariance matrix, $\mathbf{C}_\mathrm{d}$, and the modelling covariance matrix, $\mathbf{C}_\mathrm{p}$. The latter class of uncertainty is often entirely ignored even though prediction errors scale with the size of earthquakes and are thus generally larger than the observation uncertainty for large events. Furthermore, prediction errors can induce important correlation between the observation points that should be taken into account in source inversion problems. This work provides a general formalism to explicitly quantify the impact of uncertainties in our forward models and to account for such prediction error in source estimation problems. In particular, we describe a physically based stochastic model for the prediction uncertainty that allows for inaccuracies in the earth model by using sensitivity of the data predictions to first-order perturbations of elastic properties. Moreover, to account for the dependence of the prediction error upon the source model parameters $\mathbf{m}$, the covariance matrix $\mathbf{C}_\mathrm{p}$ is updated as the model evolves in the source inversion process. We also discuss the possibility to account for other sources of uncertainty such as imperfections in the fault geometry.

For a simple 2-D synthetic data inversion, we demonstrated the importance and feasibility of implementing $\mathbf{C}_\mathrm{p}$ in source inversion problems. The results indicate two main advantages of using an improved covariance matrix structure. First, it improves the posterior error description for the source model parameters. Secondly, it improves the source model characterization itself notably because using a more structured covariance matrix prevents overfitting of the observations. Although our implementation is based on a Bayesian formulation of the inversion problem, it should be noted that incorporating $\mathbf{C}_\mathrm{p}$ can be beneficial regardless of the particular inversion approach used. Indeed, the prediction covariance matrix offers a natural way to specify the relative information content found in different observations. Furthermore, if different data types are used, $\mathbf{C}_\mathrm{p}$ provides a physical basis for the relative weighting between disparate data sets.

The advances proposed here can thus enable production of the next generation of source models that are more resistant to overfitting of data, provide a physical basis for the relative weighting between disparate data sets, and include more realistic description of uncertainty in the inferred source model parameters. These improvements in the model prediction uncertainty require developing computationally tractable approaches to estimate the sensitivity of the predicted geodetic and seismic observations of large earthquakes to perturbations in material properties assumed in any given earth model. Much of the underlying theory and many of the tools already exist in the domain of seismic tomography and could thus be exploited to obtain more reliable images of the earthquake rupture phenomena. While this work is motivated by specific goals related to the study of large earthquakes, these techniques can also be applied to a broad range of inverse problems in geophysics and

earthquake engineering such as volcano monitoring and earthquake early warning.

ACKNOWLEDGEMENTS

We thank Bernard Valette and Yukitoshi Fukahata for their helpful reviews. We have benefited from discussions with Jean-Paul Ampuero, Jean Virieux, Romain Brossier, Victor Tsai, Romain Jolivet and Luis Rivera. MS acknowledges sabbatical support from the Univ. Joseph Fourier (Grenoble, France) during which this project started. PSA was supported by the Keck Institute of Space Studies Postdoctoral Fellowship. Our Bayesian sampling algorithm is based on the ALTAR implementation of CATMIP developed by Michael Aivasis and Hailiang Zhang. This work made use of the Matplotlib python library created by John D. Hunter. P. Agram was supported by the Keck Institute of Space Studies Postdoctoral Fellowship. This research was supported by the Southern California Earthquake Center. SCEC is funded by NSF Cooperative Agreement EAR-0529922 and USGS Cooperative Agreement 07HQAG0008. The SCEC contribution number for this paper is 1791. This work was partially supported by the National Science Foundation under Grant No. EAR-0941374.

REFERENCES

Aki, K. & Richards, P., 2002. *Quantitative Seismology,* Freeman.

Barnhart, W.D. & Lohman, R.B., 2010. Automated fault model discretization for inversions for coseismic slip distributions, *J. geophys. Res.,* **115**(B10), B10419, doi:10.1029/2010JB007545.

Bayes, M., 1763. An essay towards solving a problem in the doctrine of chances by the late Rev. Mr. Bayes, F.R.S. communicated by Mr. Price, in a letter to John Canton, A.M.F.R.S., *Phil. Trans. R. Soc.,* **53,** 370–418.

Beck, J.L. & Au, S.K., 2002. Bayesian updating of structural models and reliability using Markov chain Monte Carlo simulation, *J. Eng. Mech.,* **128,** 380–391.

Beck, J.L. & Zuev, K.M., 2013. Asymptotically independent Markov sampling: a new Markov chain Monte Carlo scheme for Bayesian inference, *Int. J. Uncertainty Quantification,* **3**(5), 445–474.

Bishop, C.M., 2006. *Pattern Recognition and Machine Learning,* Information Science and Statistics, Springer.

Bonnet, M. & Constantinescu, A., 2005. Inverse problems in elasticity, *Inverse Probl.,* **21**(2), R1–R50.

Bouchon, M., Toksoz, N.N., Karabulut, H., Bouin, M.-P., Dietrich, M., Aktar, M. & Edie, M., 2002. Space and time evolution of rupture and faulting during the 1999 Izmit (Turkey) earthquake, *Bull. seism. Soc. Am.,* **92**(1), 256–266.

Cervelli, P., Segall, P., Amelung, F., Garbeil, H., Meertens, C., Owen, S., Miklius, A. & Lisowski, M., 2002. The 12 September 1999 Upper East Rift Zone dike intrusion at Kilauea Volcano, Hawaii, *J. geophys. Res.,* **107**(B7), ECV3 1–13.

Ching, J. & Chen, Y.C., 2007. Transitional Markov chain Monte Carlo method for Bayesian model updating, model class selection, and model averaging, *J. Eng. Mech.,* **133,** 816–832.

Dahlen, F.A. & Baig, A.M., 2002. Fréchet kernels for body-wave amplitudes, *Geophys. J. Int.,* **150**(2), 440–466.

Dahlen, F.A. & Tromp, J., 1998. *Theoretical Global Seismology,* Princeton Univ. Press.

Delouis, B., Lundgren, P., Salichon, J. & Giardini, D., 2000. Joint inversion of InSAR and teleseismic data for the slip history of the 1999 Izmit (Turkey) earthquake, *Geophys. Res. Lett.,* **27**(20), 3389–3392.

Delouis, B., Giardini, D., Lundgren, P. & Salichon, J., 2002. Joint inversion of InSAR, GPS, teleseismic, and strong-motion data for the spatial and temporal distribution of earthquake slip: application to the 1999 Izmit mainshock, *Bull. seism. Soc. Am.,* **92,** 278–299.

Du, Y., Segall, P. & Gao, H., 1994. Dislocations in inhomogeneous media via a moduli perturbation approach: general formulation and two-dimensional solutions, *J. geophys. Res.,* **99**(B7), 13 767–13 779.

Duputel, Z., Rivera, L., Fukahata, Y. & Kanamori, H., 2012a. Uncertainty estimations for seismic source inversions, *Geophys. J. Int.,* **190**(2), 1243–1256.

Duputel, Z., Rivera, L., Kanamori, H. & Hayes, G., 2012b. W phase source inversion for moderate to large earthquakes (1990–2010), *Geophys. J. Int.,* **189**(2), 1125–1147.

Fukahata, Y. & Wright, T.J., 2008. A non-linear geodetic data inversion using ABIC for slip distribution on a fault with an unknown dip angle, *Geophys. J. Int.,* **173**(2), 353–364.

Hartzell, S.H. & Heaton, T.H., 1983. Inversion of strong ground motion and teleseismic waveform data for the fault rupture history of the 1979 Imperial Valley, California, earthquake, *Bull. seism. Soc. Am.,* **73**(6), 1553–1583.

Hernandez, B., Cotton, F. & Campillo, M., 1999. Contribution of radar interferometry to a two-step inversion of the kinematic process of the 1992 Landers earthquake, *J. geophys. Res.,* **104**(B6), 13 083–13 099.

Hjörleifsdóttir, V. & Ekström, G., 2010. Effects of three-dimensional Earth structure on CMT earthquake parameters, *Phys. Earth planet. Inter.,* **179,** 178–190.

Jaynes, E.T., 1983. *Papers on Probability, Statistics, and Statistical Physics,* Springer.

Jaynes, E.T., 2003. *Probability Theory: The Logic of Science,* Cambridge Univ. Press.

Ji, C., Wald, D.J. & Helmberger, D.V., 2002. Source description of the 1999 Hector Mine, California, earthquake, part I: wavelet domain inversion theory and resolution analysis, *Bull. seism. Soc. Am.,* **92**(4), 1192–1207.

Kanamori, H. & Rivera, L., 2006. Energy partitioning during an earthquake, in *Radiated Energy and the Physics of Faulting,* Geophys. Monograph Series, pp. 3–13, American Geophysical Union.

King, G., 2007. Earthquake seismology: 4.08—fault interaction, earthquake stress changes, and the evolution of seismicity, in *Treatise on Geophysics,* pp. 225–255, Elsevier.

Komatitsch, D. & Vilotte, J.-P., 1998. The spectral element method: an efficient tool to simulate the seismic response of 2D and 3D geological structures, *Bull. seism. Soc. Am.,* **88,** 368–392.

Lohman, R.B. & Simons, M., 2005. Some thoughts on the use of InSAR data to constrain models of surface deformation: noise structure and data downsampling, *Geochem. Geophys. Geosyst.,* **6**(1), Q01007, doi:10.1029/2004GC000841.

Love, A.H.E., 1906. *A Treatise on the Mathematical Theory of Elasticity,* 2nd edn, Cambridge Univ. Press.

Mai, M., 2012. Source inversion validation (SIV): current results & developments, in *Proceedings of the 2012 SCEC Source Inversion Validation Workshop,* Hilton Palm Springs Resort.

Marquering, H., Nolet, G. & Dahlen, F.A., 1998. Three-dimensional waveform sensitivity kernels, *Geophys. J. R. astr. Soc.,* **132**(3), 521–534.

Minson, S.E., Simons, M. & Beck, J.L., 2013. Bayesian inversion for finite fault earthquake source models I—theory and algorithm, *Geophys. J. Int.,* **194**(3), 1701–1726.

Minson, S.E., Simons, M., Beck, J.L., Ortega, F., Jiang, J. & Owen, S.E., 2014. Bayesian inversion for finite fault earthquake source models II—The 2011 great Tohoku-oki, Japan earthquake, *Geophys. J. Int.,* submitted.

Okada, Y., Kasahara, K., Hori, S. & Obara, K., 2004. Recent progress of seismic observation networks in Japan-Hi-net, F-net, K-NET and KiK-net, *Earth Planets Space,* **56,** 15–28.

Pritchard, M.E., Simons, M., Rosen, P.A., Hensley, S. & Webb, F.H., 2002. Co-seismic slip from the 1995 July 30 Mw= 8.1 Antofagasta, Chile, earthquake as constrained by InSAR and GPS observations, *Geophys. J. Int.,* **150**(2), 362–376.

Pritchard, M.E., Norabuena, E.O., Ji, C., Boroschek, R., Comte, D., Simons, M., Dixon, T.H. & Rosen, P.A., 2007. Geodetic, teleseismic, and strong motion constraints on slip from recent southern Peru subduction zone earthquakes, *J. geophys. Res.,* **112**(B3), B03307, doi:10.1029/2006JB004294.

Rice, J.R. & Cocco, M., 2007. Seismic fault rheology and earthquake dynamics, in *Tectonic Faults: Agents of Change on a Dynamic Earth (Dahlem Workshop Reports),* pp. 99–137, MIT Press.

Savage, J.C., 1987. Effect of crustal layering upon dislocation modeling, *J. geophys. Res.,* **92**(B10), 10 595–10 600.

Segall, P., 2010. *Earthquake and Volcano Deformation,* Princeton Univ. Press.
Sekiguchi, H. & Iwata, T., 2002. Rupture process of the 1999 Kocaeli, Turkey, earthquake estimated from strong-motion waveforms, *Bull. seism. Soc. Am.,* **92**(1), 300–311.
Simons, M. & Rosen, P.A., 2007. Interferometric synthetic aperture radar geodesy, in *Treatise on Geophysics,* pp. 391–446, Elsevier.
Simons, M. *et al.*, 2011. The 2011 magnitude 9.0 Tohoku-Oki earthquake: mosaicking the megathrust from seconds to centuries, *Science,* **332**(6036), 1421–1425.
Talagrand, O. & Courtier, P., 2007. Variational assimilation of meteorological observations with the adjoint vorticity equation. I: theory, *Q. J. R. Meteorol. Soc.,* **113**(478), 1311–1328.
Tarantola, A., 1984. Inversion of seismic reflection data in the acoustic approximation, *Geophysics,* **49**(8), 1259–1266.
Tarantola, A., 1988. Theoretical background for the inversion of seismic waveforms including elasticity and attenuation, *Pure appl. geophys.,* **128**(1–2), 365–399.
Tarantola, A., 2005. *Inverse Problem Theory and Methods for Model Parameter Estimation,* SIAM.
Tarantola, A. & Valette, B., 1982. Inverse problems = quest for information, *J. Geophys.,* **50,** 159–170.
Tromp, J., Tape, C. & Liu, Q., 2005. Seismic tomography, adjoint methods, time reversal and banana-doughnut kernels, *Geophys. J. Int.,* **160**(1), 195–216.
Virieux, J. & Operto, S., 2009. An overview of full-waveform inversion in exploration geophysics, *Geophysics,* **74,** WCC1–WCC26.
Wald, D.J. & Heaton, T.H., 1994. Spatial and temporal distribution of slip for the 1992 Landers, California, earthquake, *Bull. seism. Soc. Am.,* **84,** 668–691.
Williams, C.A., Aagaard, B. & Knepley, M.G., 2005. Development of software for studying earthquakes across multiple spatial and temporal scales by coupling quasi-static and dynamic simulations, *EOS, Trans. Am. geophys. Un.,* **86,** AGU abstract #S53A–1072.
Yabuki, T. & Matsu'ura, M., 1992. Geodetic data inversion using a Bayesian information criterion for spatial distribution of fault slip, *Geophys. J. Int.,* **109,** 363–375.
Yagi, Y. & Fukahata, Y., 2011. Introduction of uncertainty of Green's function into waveform inversion for seismic source processes, *Geophys. J. Int.,* **186**(2), 711–720.
Yagi, Y. & Kikuchi, M., 2000. Source rupture process of the Kocaeli, Turkey, earthquake of August 17, 1999, obtained by joint inversion of near-field data and teleseismic data, *Geophys. Res. Lett.,* **27**(13), 1969–1972.
Yu, S.-B., Chen, H.-Y. & Kuo, L.-C., 1997. Velocity field of GPS stations in the Taiwan area, *Tectonophysics,* **274,** 41–59.

APPENDIX A: POSTERIOR PROBABILITY DENSITY FUNCTION (PDF) UNDER THE ASSUMPTION OF GAUSSIAN UNCERTAINTIES

Under the Gaussian assumption, we demonstrate that the posterior PDF is given by eq. (8) of the main text. We essentially follow the demonstration originally given by Tarantola & Valette (1982) in the more general case when $\mathbf{C}_\mathrm{p}$ depends on $\mathbf{m}$. If $p(\mathbf{d}^*|\mathbf{d})$ and $p(\mathbf{d}|\mathbf{m})$ are assumed to be Gaussian PDFs as in eqs (2) and (4), the integrated likelihood in eq. (7) is proportional to the convolution between two Gaussians:

$$p(\mathbf{d}_\mathrm{obs}|\mathbf{m}) = \nu(\mathbf{m}) \int_{\mathfrak{D}_\mathrm{pred}} \exp\left(-\frac{1}{2}\left\{(\mathbf{d}_\mathrm{obs}-\mathbf{d})^T\ \mathbf{C}_\mathrm{d}^{-1}\ (\mathbf{d}_\mathrm{obs}-\mathbf{d}) + \left[\mathbf{d}-\mathbf{g}(\widetilde{\mathbf{\Omega}},\mathbf{m})\right]^T\ \mathbf{C}_\mathrm{p}(\mathbf{m})^{-1}\left[\mathbf{d}-\mathbf{g}(\widetilde{\mathbf{\Omega}},\mathbf{m})\right]\right\}\right) \mathrm{d}\mathbf{d}, \tag{A1}$$

where $\nu(\mathbf{m})$ is a normalization factor defined as

$$\nu(\mathbf{m}) = (2\pi)^{-N}\ |\mathbf{C}_\mathrm{d}|^{-1/2}\left|\mathbf{C}_\mathrm{p}(\mathbf{m})\right|^{-1/2}. \tag{A2}$$

Eq. (A1) can be rearranged by separating quadratic terms from the linear terms

$$p(\mathbf{d}_\mathrm{obs}|\mathbf{m}) = \nu \int_{\mathfrak{D}_\mathrm{pred}} \exp\left(-\frac{1}{2}\left(\mathbf{d}^T\ \mathbf{A}\,\mathbf{d} - 2\,\mathbf{b}^T\,\mathbf{d} + c\right)\right) \mathrm{d}\mathbf{d}, \tag{A3}$$

where we define

$$\begin{aligned}\mathbf{A} &= \mathbf{C}_\mathrm{d}^{-1} + \mathbf{C}_\mathrm{p}(\mathbf{m})^{-1}\\ \mathbf{b}^T &= \mathbf{d}_\mathrm{obs}^T\mathbf{C}_\mathrm{d}^{-1} + \mathbf{g}(\widetilde{\mathbf{\Omega}},\mathbf{m})^T\mathbf{C}_\mathrm{p}(\mathbf{m})^{-1}\\ c &= \mathbf{d}_\mathrm{obs}^T\mathbf{C}_\mathrm{d}^{-1}\mathbf{d}_\mathrm{obs} + \mathbf{g}(\widetilde{\mathbf{\Omega}},\mathbf{m})^T\mathbf{C}_\mathrm{p}(\mathbf{m})^{-1}\mathbf{g}(\widetilde{\mathbf{\Omega}},\mathbf{m}).\end{aligned} \tag{A4}$$

The matrix $\mathbf{A}$ being positive definite, we can then show

$$p(\mathbf{d}_\mathrm{obs}|\mathbf{m}) = \nu\ \exp\left(-\frac{1}{2}\left(c-\mathbf{b}^T\mathbf{A}^{-1}\mathbf{b}\right)\right) \times \int_{\mathfrak{D}_\mathrm{pred}} \exp\left(-\frac{1}{2}\left(\mathbf{d}-\mathbf{A}^{-1}\mathbf{b}\right)^T\mathbf{A}\left(\mathbf{d}-\mathbf{A}^{-1}\mathbf{b}\right)\right) d\mathbf{d}. \tag{A5}$$

The integral of the Gaussian in the right and side being equal to $\sqrt{(2\pi)^N/|\mathbf{A}|}$, it follows that

$$p(\mathbf{d}_\mathrm{obs}|\mathbf{m}) = \eta\ \exp\left(-\frac{1}{2}\left(c-\mathbf{b}^T\,\mathbf{A}^{-1}\,\mathbf{b}\right)\right) \tag{A6}$$

where

$$\eta(\mathbf{m}) = (2\pi)^{-N/2}\ |\mathbf{C}_\mathrm{d}|^{-1/2}\left|\mathbf{C}_\mathrm{p}(\mathbf{m})\right|^{-1/2}\left|\mathbf{C}_\mathrm{d}^{-1}+\mathbf{C}_\mathrm{p}(\mathbf{m})^{-1}\right|^{-1/2}. \tag{A7}$$

After substituting eqs (A4) into (A6) and using the following identities (Tarantola & Valette 1982)

$$\begin{aligned}\left[\mathbf{C}_\mathrm{d}+\mathbf{C}_\mathrm{p}(\mathbf{m})\right]^{-1} &= \mathbf{C}_\mathrm{d}^{-1} - \mathbf{C}_\mathrm{d}^{-1}\left[\mathbf{C}_\mathrm{d}^{-1}+\mathbf{C}_\mathrm{p}(\mathbf{m})^{-1}\right]^{-1}\mathbf{C}_d^{-1}\\ &= \mathbf{C}_\mathrm{p}^{-1} - \mathbf{C}_\mathrm{p}(\mathbf{m})^{-1}\left[\mathbf{C}_\mathrm{d}^{-1}+\mathbf{C}_\mathrm{p}(\mathbf{m})^{-1}\right]^{-1}\mathbf{C}_\mathrm{p}(\mathbf{m})^{-1}\\ &= \mathbf{C}_\mathrm{p}(\mathbf{m})^{-1}\left[\mathbf{C}_\mathrm{d}^{-1}+\mathbf{C}_\mathrm{p}(\mathbf{m})^{-1}\right]^{-1}\mathbf{C}_\mathrm{d}^{-1}\end{aligned} \tag{A8}$$

we then obtain

$$p(\mathbf{d}_\mathrm{obs}|\mathbf{m}) = \eta(\mathbf{m})\exp\left(-\frac{1}{2}\left[\mathbf{d}_\mathrm{obs}-\mathbf{g}(\widetilde{\mathbf{\Omega}},\mathbf{m})\right]^T \times \left(\mathbf{C}_\mathrm{d}+\mathbf{C}_\mathrm{p}\right)^{-1}\left[\mathbf{d}_\mathrm{obs}-\mathbf{g}(\widetilde{\mathbf{\Omega}},\mathbf{m})\right]\right), \tag{A9}$$

which demonstrates eq. (8) of Section 2.

APPENDIX B: SENSITIVITY KERNEL $\mathbf{K}_\mu$ IN THE QUASI-STATIC CASE FOR GENERAL 3-D PERTURBATIONS

We describe here the formulation of $\mathbf{K}_\mu$ for the case of a known source and a set of distributed receivers. We adopt a perturbation approach which has been extensively used in seismic (e.g. Dahlen & Baig 2002; Virieux & Operto 2009) and quasi-static problems (Du *et al.* 1994; Cervelli *et al.* 2002). Assuming that the earth model is characterized by the elastic stiffness tensor c_{ijkl}, for a given source field $f(x)$ and a set of boundary conditions, the predicted displacement field is described by the equation (Love 1906;

Segall 2010)

$$\frac{\partial}{\partial x_j}\left[c_{ijkl}(\mathbf{x})\,\frac{\partial u_k}{\partial x_l}(\mathbf{x})\right] + f_i(\mathbf{x}) = 0, \tag{B1}$$

where the Einstein summation convention applies to repeated subscript indices. Introducing the Green's function $H_{ij}(\mathbf{x}, \mathbf{x}^s)$, the solution of this equation can be written in the integral form

$$u_i(\mathbf{x}) = \int_{V^s} H_{ij}(\mathbf{x}, \mathbf{x}^s)\; f_j(\mathbf{x}^s)\; \mathrm{d}^3\mathbf{x}^s, \tag{B2}$$

where V^s is the volume of the source region. Let us now assume that a perturbation of the earth model

$$c_{ijkl}(\mathbf{x}) \rightarrow c_{ijkl}(\mathbf{x}) + \delta c_{ijkl}(\mathbf{x}) \tag{B3}$$

leads to a perturbation of the predicted displacement field:

$$u_i(\mathbf{x}) \rightarrow u_i(\mathbf{x}) + \delta u_i(\mathbf{x}). \tag{B4}$$

To derive the displacement sensitivity to the medium elastic properties, we insert eqs (B3)–(B4) into eq. (B1) and drop second-order terms:

$$\frac{\partial}{\partial x_j}\left[c_{ijkl}(\mathbf{x})\,\frac{\partial \delta u_k}{\partial x_l}(\mathbf{x})\right] + \delta f_i(\mathbf{x}) = 0, \tag{B5}$$

where $\delta\mathbf{f}$ is defined as

$$\delta f_i(\mathbf{x}) = \frac{\partial}{\partial x_j}\left[\delta c_{ijkl}(\mathbf{x})\,\frac{\partial u_k}{\partial x_l}(\mathbf{x})\right]. \tag{B6}$$

Note that this first-order perturbation equation is equivalent to the Born approximation in elastodynamics (Dahlen & Tromp 1998; Aki & Richards 2002) where $\delta\mathbf{f}$ is the secondary Born source. Since the solution of the eq. (B1) is given by eq. (B2), the solution for $\delta\mathbf{u}$ in eq. (B5) can be expressed as

$$\delta u_m(\mathbf{x}) = \int_V H_{mi}(\mathbf{x}, \mathbf{x}')\,\frac{\partial}{\partial x_j}\left[\delta c_{ijkl}(\mathbf{x}')\,\frac{\partial u_k}{\partial x_l}(\mathbf{x}')\right]\mathrm{d}^3\mathbf{x}', \tag{B7}$$

where V denotes the earth model volume. After some manipulations using the divergence theorem, we obtain

$$\delta u_m(\mathbf{x}) = -\int_V \frac{\partial H_{mi}(\mathbf{x}, \mathbf{x}')}{\partial x'_j}\,\frac{\partial u_k}{\partial x'_l}(\mathbf{x}')\,\delta c_{ijkl}(\mathbf{x}')\,\mathrm{d}^3\mathbf{x}' + \int_S H_{mi}(\mathbf{x}, \mathbf{x}')\delta c_{ijkl}(\mathbf{x}')\frac{\partial u_k}{\partial x'_l} n_j \mathrm{d}^2\mathbf{x}', \tag{B8}$$

where n_j is the normal to the Earth's surface. The second integral vanishes because of homogeneous boundary conditions. If we assume an isotropic medium, assuming only perturbations in the shear modulus (μ) while holding the Poisson's ratio constant, we can then write

$$\delta u_i(\mathbf{x}) = -\int_V \frac{\partial H_{ij}(\mathbf{x}, \mathbf{x}')}{\partial x'_k}\,\frac{\sigma_{jk}(\mathbf{x}')}{\mu(\mathbf{x}')}\,\delta\mu(\mathbf{x}')\,\mathrm{d}^3\mathbf{x}', \tag{B9}$$

where $\sigma_{ij}(\mathbf{x}') = c_{ijkl}(\mathbf{x}')u_{k,l}(\mathbf{x}')$. For practical implementation, we can discretize the elastic medium into a limited number of layers (as done in Section 4) or tectonically parametrized regions (e.g. crust, mantle). If we allow for piecewise variation of μ in such regions, we can then simplify eq. (B9) using again the divergence theorem to obtain the following 2-D surface integral (Du *et al.* 1994)

$$\delta u_i(\mathbf{x}) = -\sum_r \delta \ln \mu^r \int_{S^r} H_{ij}(\mathbf{x}, \mathbf{x}')\,\sigma_{jk}(\mathbf{x}')\,n_k^r(\mathbf{x}')\,\mathrm{d}^2\mathbf{x}', \tag{B10}$$

where $n_k^r(\mathbf{x}')$ is the normal to the surface S^r delimiting the rth perturbed region. From this equation, we can directly extract the shear modulus sensitivity kernel $\mathbf{J}_\mu$ of the predicted displacement field $\mathbf{u}(\mathbf{x})$ for the rth layer or tectonic region

$$(\mathbf{J}_\mu)_i^r(\mathbf{x}) = -\int_{S^r} H_{ij}(\mathbf{x}, \mathbf{x}')\,\sigma_{jk}(\mathbf{x}')\,n_k(\mathbf{x}')\,\mathrm{d}^2\mathbf{x}'. \tag{B11}$$

Recognizing the fact that geodetic predictions ($\mathbf{d}_{\mathrm{pred}}$) represent only a subset of the total predicted displacement field, we can write

$$\mathbf{d}_{\mathrm{pred}} = \mathbf{R}\cdot\mathbf{u}, \tag{B12}$$

where $\mathbf{R}$ is a sampling operator acting on the complete displacement field $\mathbf{u}(\mathbf{x})$. Similarly, the integral form in eq. (B10) can be discretized to express the model prediction uncertainty ($\boldsymbol{\epsilon}$) as

$$\begin{aligned}\boldsymbol{\epsilon} &= \mathbf{R}\cdot\delta\mathbf{u}\\ &= \mathbf{R}\cdot\mathbf{J}_\mu\cdot\delta\ln\boldsymbol{\mu}.\end{aligned} \tag{B13}$$

From the definition of $\boldsymbol{\epsilon}$ in eq. (14) of Section 3.1, we can then write the sensitivity kernel as

$$\mathbf{K}_\mu = \mathbf{R}\cdot\mathbf{J}_\mu. \tag{B14}$$

SUPPORTING INFORMATION

Additional Supporting Information may be found in the online version of this article :

Figure S1. Source estimation for a constant unit slip distribution if $\mathbf{C}_\mathrm{p}$ is neglected.

Figure S2. One-dimensional marginal posterior PDFs for each patch as a function of depth. The marginal probability density histograms are shown in green (a) when the prediction uncertainty is neglected and (b) when the prediction uncertainty is taken into account by including $\mathbf{C}_\mathrm{p}$ in the inversion problem. The target slip model is indicated as dashed black lines and mean of the distribution is shown in blue. The results in (b) are obtained using approach (2) described in Section 4.4 of the main text: $\mathbf{C}_\mathrm{p}$ is calculated at $\beta = 0$ assuming a uniform unitary slip distribution as a function of depth (*cf.* model shown in Fig. S4 for $\beta = 0$).

Figure S3. Evolution of the prediction covariance $\mathbf{C}_\mathrm{p}$ at each transitional step. The approach (3) described in Section 4.4 of the main text is used here: $\mathbf{C}_\mathrm{p}$ is calculated at $\beta = 0$ assuming a uniform unitary slip distribution as a function of depth (*cf.* model shown in Fig. S4 for $\beta = 0$).

Figure S4. Slip models used for the calculation of the prediction covariance $\mathbf{C}_\mathrm{p}$. The approach (3) described in Section 4.4. of the main text is used here: the model used for the calculation of $\mathbf{C}_\mathrm{p}$ at $\beta = 0$ assuming a uniform unitary slip distribution as a function of depth (*cf.* model shown for $\beta = 0$).

Figure S5. One-dimensional marginal posterior PDFs for each patch as a function of depth. The marginal probability density histograms are shown in green (a) when the prediction uncertainty is neglected and (b) when the prediction uncertainty is taken into account by including $\mathbf{C}_\mathrm{p}$ in the inversion problem. The target slip model is indicated as dashed black lines and mean of the distribution is shown in blue. The results in (b) are obtained using approach (3) described in Section 4.4 of the main text: $\mathbf{C}_\mathrm{p}$ is calculated at $\beta = 0$ using the posterior mean model for which $\mathbf{C}_\mathrm{p}$ is neglected (*cf.* blue bars in (a) and Fig. S7).

Figure S6. Evolution of the prediction covariance $\mathbf{C}_\mathrm{p}$ at each transitional step. The approach (3) described in Section 4.4. of the main text is used here: $\mathbf{C}_\mathrm{p}$ is calculated at $\beta = 0$ using the posterior mean model for which $\mathbf{C}_\mathrm{p}$ was neglected (*cf.* Fig. S7 and blue bars in Fig. S5a).

Figure S7. Slip models used for the calculation of the prediction covariance $\mathbf{C}_\mathrm{p}$. The approach (3) described in Section 4.4. of the main text is used here: the model used for the calculation of $\mathbf{C}_\mathrm{p}$ at $\beta = 0$ is the posterior mean model when $\mathbf{C}_\mathrm{p}$ is neglected (*cf.* blue bars in Fig. S5a).

Figure S8. One-dimensional marginal posterior PDFs for each patch as a function of depth. The marginal probability density histograms are shown in green (a) when the prediction uncertainty is neglected and (b) when the prediction uncertainty is taken into account by including $\mathbf{C}_\mathrm{p}$ in the inversion problem. The target slip model is indicated as dashed black lines and mean of the distribution is shown in blue. The results in (b) are obtained using approach (4) described in Section 4.4 of the main text: We use a preliminary form of $\mathbf{C}_\mathrm{p}$ whose diagonal elements are proportional to observations.

Figure S9. Evolution of the prediction covariance $\mathbf{C}_\mathrm{p}$ at each transitional step. At $\beta = 0$, we use a preliminary form of $\mathbf{C}_\mathrm{p}$ whose diagonal elements are proportional to observations (*cf.* approach (4) described in Section 4.4 of the main text).

Figure S10. Slip models used for the calculation of the prediction covariance $\mathbf{C}_\mathrm{p}$. We use a preliminary form of $\mathbf{C}_\mathrm{p}$ whose diagonal elements are proportional to observations (*cf.* approach (4) described in Section 4.4 of the main text).

Figure S11. Same as Fig. 7 in the main text but using strictly positive constraints with a prior $p(\mathbf{m}) = \mathcal{U}(0, 20)^M$ (http://gji.oxfordjournals.org/lookup/suppl/doi:10.1093/gji/ggt517/-/DC1).